Revista Mexicana de Astronomía y Astrofísica, **59**, 213–258 (2023)

https://doi.org/10.22201/ia.01851101p.2023.59.02.06

SDSS-IV MANGA: THE RADIAL DISTRIBUTION OF PHYSICAL PROPERTIES WITHIN GALAXIES IN THE NEARBY UNIVERSE

J. K. Barrera-Ballesteros[1], S. F. Sánchez[1], C. Espinosa-Ponce[1], C. López-Cobá[2], L. Carigi[1], A. Z. Lugo-Aranda[1], E. Lacerda[1], G. Bruzual[3], H. Hernandez-Toledo[1], N. Boardman[4], N. Drory[5], Richard R. Lane[6], and J. R. Brownstein[7]

Received May 26 2022; accepted May 25 2023

ABSTRACT

Using the largest sample of galaxies observed with an optical integral field unit (IFU, the SDSS-IV MaNGA survey, ≈10000 targets), we derive the radial distribution of the physical properties obtained from the stellar continuum and the ionized-gas emission lines. Given the large sample, we are able to explore the impact of the total stellar mass and morphology by averaging those radial distributions for different bins of both global properties. In general, we find that most of the properties exhibit a negative gradient, with a secondary impact by global properties. Our results confirm the intimate interplay between the properties of the stellar component and those of the ionized gas at local (kpc) scales to set the observed radial gradients. The resemblance of the gradients for similar global properties indicates statistical similar histories of star formation and chemical enrichment, with an initial radial gas distribution following the potential of the galaxy.

RESUMEN

Usando la muestra más grande de galaxias con observaciones espacialmente resueltas (el cartografiado SDSS-IV MaNGA, ≈10000 objetos) estimamos las distribuciones radiales de las propiedades obtenidas a través del continuo y de las líneas de emisión del espectro óptico. La muestra permite explorar el impacto que parámetros como la masa estelar total y la morfología tienen en los gradientes. De manera general, encontramos que la mayoría de las propiedades muestran un gradiente cuya pendiente es negativa con un impacto secundario de la masa estelar y la morfología. Nuestros resultados confirman la relación entre las propiedades de las estrellas con el gas ionizado a escalas locales (kpc), las cuales fijan los perfiles radiales observados. Las similitud entre gradientes para galaxias con propiedades similares indican historias de formación estelar y enriquecimiento químico parecidas con una distribución inicial de gas que sigue el potencial de la galaxia.

Key Words: galaxies: fundamental parameters — galaxies: stellar content — surveys — techniques: spectroscopic

1. INTRODUCTION

Projected on the sky, galaxies are spatially resolved objects. To truly assess the physical processes that drive the galaxy formation and evolution it is necessary to measure their observables in a spatially-resolved fashion. One of the most well-known techniques to estimate structural properties of a galaxy is through the measurement and fitting of its surface brightness radial profile (e.g., de Vaucouleurs 1958; Sersic 1968; Freeman 1970; Kormendy 1977; Kent 1985). In general, the surface brightness (from broad-band photometry) decreases with radius, in-

[1]Universidad Nacional Autónoma de México, Instituto de Astronomía, CDMX, México.
[2]Institute of Astronomy and Astrophysics, Academia Sinica, Taipei, Taiwan.
[3]IRyA, Universidad Nacional Autónoma de México, Campus Morelia, Michoacán, México.
[4]School of Physics and Astronomy, University of St Andrews, UK.
[5]University of Texas at Austin, McDonald Observatory, Austin, TX, USA.
[6]Centro de Investigación en Astronomía, Universidad Bernardo O'Higgins, Santiago, Chile.
[7]Department of Physics and Astronomy, University of Utah, UT, USA.

dicating that the amount of stars is larger in the central regions of galaxies.

Similarly, there are studies exploring the radial profiles of the Hα emission line using narrow-band filters (e.g., Martin & Kennicutt 2001; Bigiel et al. 2008). Although the Hα emission usually is small in the outskirts in comparison to central regions, these studies showed that not for all galactocentric distances the Hα emission monotonically decreases with radius. Long-slit spectroscopy has also been a powerful tool to measure the radial distributions of physical properties from both the stellar continuum and the ionized gas emission lines (e.g., Pagel & Edmunds 1983; Peletier 1989). Through the analysis of different features of the stellar absorption lines and emission lines, such studies have provided a new way to estimate physical properties from each component at different galactocentric distances (e.g., stellar ages, and metallicities; star-formation rates, oxygen abundances, among many others).

Despite these significant efforts, these studies have been performed in samples of galaxies targeted to explore a specific scientific goal. Furthermore, the above techniques do not fully capture the angular distribution of the observables from both components. These issues have been successfully overcome thanks to large samples of galaxies observed using the Integral Field Spectroscopy (IFS) technique. This observational technique allows to obtain spectra for different positions of a galaxy across its optical extension. Thus, for each of the physical parameters derived from spectroscopy, it is possible to estimate a two-dimensional distribution. Different collaborations have acquired IFS datacubes for large samples of galaxies (e.g., Sánchez et al. 2012; Croom et al. 2012, CALIFA, and SAMI). Of particular interest is the MaNGA survey included in the SDSS-IV collaboration (Bundy et al. 2015). This collaboration has recently achieved its goal to observe a sample of 10000 galaxies using an integral field unit (IFU). Given the large sample probed by these surveys, they have unveiled the radial distribution of physical properties for a wide demographic range of galaxies in the local universe for both the stellar and ionized gas components. In particular, these surveys allow us to quantify the impact that global and structural parameters, such as the total stellar mass or the morphology, have in modulating the slopes and absolute values of those radial profiles (see Sánchez 2020, and references therein).

In this study we explore the radial distribution of physical parameters from the stellar and ionized gas component using the entire MaNGA dataset. Our goal is to quantify the impact that global parameter have in shaping the radial profiles of those properties. Furthermore, to give a more accurate description than a single gradient for those profiles will provide, we make use of a piece-wise analysis which allows us to measure different slopes and breaks for a given radial distribution of a physical property. In § 2 we provide a brief description of the MaNGA sample, the IFU datacubes, and the analysis pipeline used to estimate the map for a given observable. In this section we describe the criteria to select a set of the closest galaxies with the best spatial coverage and physical spatial resolution from which we will derive their radial profiles (known as *Golden Sample*). We also describe the piece-wise analysis to measure the slopes of those profiles. In § 3 and § 4 we present the piece-wise analysis of the radial distribution of the properties derived from the stellar and ionized gas components, respectively. In § 5 we present the radial distribution of the line-of-sight velocity and velocity dispersion from both components, as well as comparisons between them. In § 6 we compare the results from § 3 and § 4 with those using the entire sample of MaNGA galaxies (excluding only highly-inclined targets, $\approx$ 7000 galaxies). Finally, in § 8 we summarize our main results and conclusions.

2. SAMPLE, DATACUBES, AND ANALYSIS

2.1. *The MaNGA Survey*

The MaNGA survey (Bundy et al. 2015) was part of the forth generation of surveys included in the Sloan Digital Sky Survey (SDSS-IV, Blanton et al. 2017). The goal of this spectroscopic survey was to obtain datacubes in the optical for more than 10000 galaxies via IFU observations. The final sample includes galaxies observed from March of 2014 to September of 2020 (10245 unique datacubes). This sample is publicly available in the final data release of the SDSS-IV surveys (Abdurro'uf et al. 2021). For this study we use the latest MaNGA data release (v3.1.1). In this section we provide a brief description of the most relevant features of this survey.

Observations for the MaNGA survey took place at the Apache Point Observatory using its 2.5-m telescope (Gunn et al. 2006). This survey used two spectrographs from the BOSS survey (Baryon Oscillation Spectroscopic Survey, Smee et al. 2013). These spectrographs achieve a nominal spectral resolution of $R \equiv \lambda/\Delta\lambda \approx 1900$ covering a large portion of the optical spectra (from 3000 to 10000 Å). These spectrographs were fed by joined fibers in bundles distributed in a hexagon-like array. The number of fibers in a given bundle varies from 19 to 127. Given

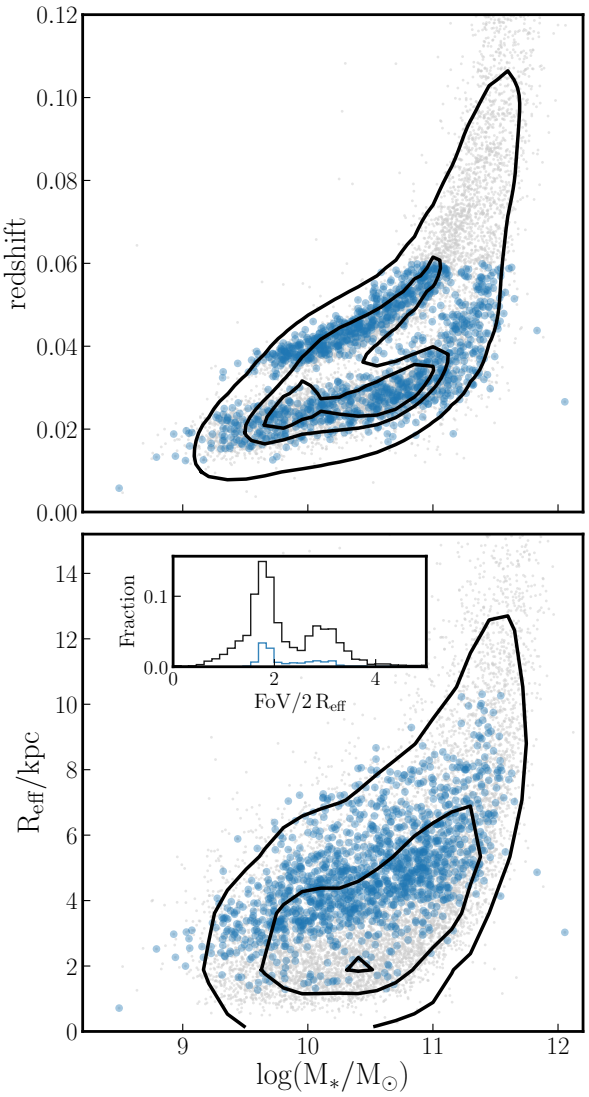

Fig. 1. Comparing the Golden Sample (GS) with its parent, the MaNGA sample according to their distance (redshift), size ($R_{\rm eff}$) and stellar mass, M_* (top and bottom panels, respectively). The gray points represent the entire MaNGA survey, while the contours enclose 90%, 80%, and 50% of this sample. The blue circles represent the GS. The inset in the bottom panel shows the distribution of the radial coverage of both samples. The spatial-resolution criteria required to drawn the GS reduces its size to ≈10% the entire MaNGA survey (see details in § 2.2). The color figure can be viewed online.

that the diameter of each fiber is ≈ 2.5″, thus the field-of-view (FoV) varies from 12″to 32″. A detailed description of the instrumentation of the survey can be found in Drory et al. (2015). The reader is refereed to Law et al. (2016) for a detailed explanation of the data strategy (acquisition, reduction, etc). The MaNGA reduction pipeline includes wavelength calibration, corrections from fiber-to-fiber transmission, subtraction of the sky spectrum and flux calibration (Yan et al. 2016). The final product is a datacube with x and y coordinates corresponding to the sky coordinates and the z-axis corresponds to the wavelength. As result for each datacube, the spaxel size is 0.5″ with a spatial resolution of 2.5″ corresponding to a mean physical scale of ≈ 2 kpc.

In Figure 1 the contours show the distribution of the entire MaNGA sample in three fundamental parameters, their redshift (z), size ($R_{\rm eff}$), and total stellar mass (M_*)[8]. From the top panel of Figure 1 it is evident that this sample covers both a wide range in redshift and M_* ($0.01 < z < 0.14$ and $9.0 < \log(M_*/{\rm M}_\odot) < 11.5$, respectively). A wide coverage of redshift implies a large dynamical range in the physical spatial resolution of the survey. The strong correlation between these two parameters is also clear: massive galaxies are located further away from us than low-mass galaxies. Furthermore, the MaNGA sample shows a bimodality in this plane. This is a result of the intrinsic selection criteria of the survey where ≈ 2/3 of the sample is selected in a way that for each galaxy the fiber bundle covers at least 1.5 $R_{\rm eff}$, for the remaining fraction of the sample, the bundle covers ≈ 2.5 $R_{\rm eff}$ for each galaxy. Thus, to satisfy this criterion, for a given range of M_* the sample has a fraction of galaxies closer and another further away from us. The bottom panel of Figure 1 shows an expected behavior of $R_{\rm eff}$ with M_*: massive galaxies are bigger in comparison to low-mass ones. The distribution of the FoV weighted by $R_{\rm eff}$ shows the bimodality presented in the z-M_* plane (see inset in bottom panel of Figure 1). The reader is addressed to Wake et al. (2017) for a detailed description of the selection criteria for the MaNGA survey.

The statistical strength of this survey allows us to explore not only the spatially resolved properties of individual galaxies but also their integrated properties. In Figure 2 we show the integrated star formation rate (SFR) against the M_* for the entire MaNGA sample (black contours and gray points). The distribution of this sample in the SFR-M_* plane shows the bimodality observed in larger samples of galaxies using integrated properties. We note that a significant fraction of galaxies are located in the so-called 'Star-Formation Main Sequence' (SFMS, e.g., Brinchmann et al. 2004; Renzini & Peng 2015), that

[8]A full description of the integrated properties derived from the IFU datacubes for the entire MaNGA survey is presented in Sanchez et al. (submitted).

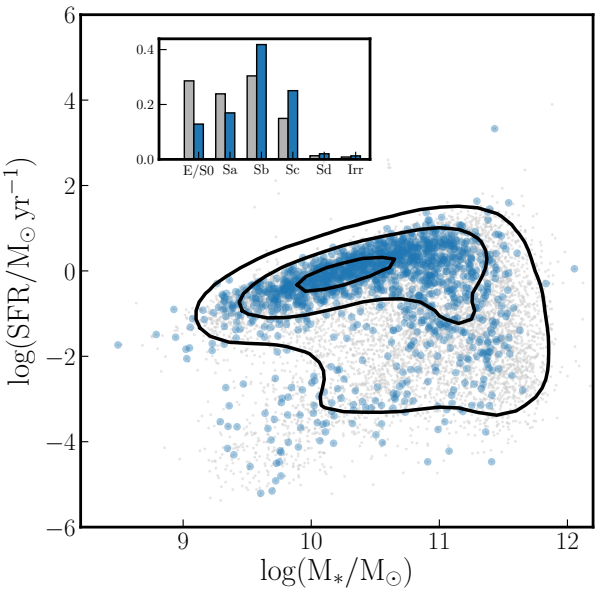

Fig. 2. Comparison of the Golden Sample and the entire MaNGA sample in the SFR-M_* plane. As in the previous figure, the blue points represent the golden sample whereas the gray points and the contours represent the MaNGA sample. The blue bars in the histogram in the inset shows the number of galaxies for a given morphology for the golden sample while the gray bars show the morphological distribution for the entire sample. Given our selection criteria from the golden sample, it includes a significant fraction of star-forming Sb galaxies in comparison to the MaNGA sample. The color figure can be viewed online.

is, galaxies that actively form new stars. The remaining fraction of the sample occupy the so-called 'Retired-Galaxies Sequence' (RGS), galaxies with little or no formation of new stars, and the so-called Green Valley, that is, galaxies located in the middle of the SFMS and the RGS in the SFR-M_* plane. Finally, when we study the morphological distribution of the MaNGA survey we find that this sample covers a wide range of morphological types from early to late types (see inset in Figure 2). In a dedicated article on the integrated properties of the MaNGA survey, Sanchez et al. (submitted) present a detailed description and analysis of the above properties.

2.2. *Sample Selection: The Golden Sample*

The main goal of this work is to explore the radial distribution of the properties of galaxies using the MaNGA survey. Therefore, we require to have a sample in which the fiber bundle of the MaNGA instrumentation provides a good spatial coverage for each of the galaxies in the sample (Ibarra-Medel et al. 2019). From the MaNGA sample we select a sub-sample of galaxies according to the following criteria: (*i*) galaxies observed with the largest fiber bundles (i.e., 91 and 127 fibers); (*ii*) the effective diameter of the galaxy (i.e., 2 $R_{\rm eff}$) has to be larger than 2 times the spatial resolution (≈5″); (*iii*) the FoV has to cover at least 3.5 times the effective diameter (this is motivated from the distribution of the sample in the coverage of the MaNGA FoV, see inset in Figure 1); (*iv*) the major/minor axis ratio has to be smaller than 0.45; and (*v*) the redshift of the galaxy has to be in the range $0.005 < z < 0.06$. The above selection criteria ensure that we select galaxies with a reliable coverage of the galaxy as well as a significant independent data within each galaxy. In particular, the selection criteria (*v*) ensures that within this sample we are considering a consistent physical spatial resolution and that the evolution of the galaxies is similar. These criteria yield a final sample of 1347 galaxies, representing ≈ 13% of the total MaNGA sample. We are referring to this sample in this article as the *Golden Sample (GS)*. Although we could impose more restrictive selection criteria to obtain the GS, this would lead to a sub-sample that it is not representative of the entire MaNGA population.

We overplot the GS in Figures 1 and 2 (blue circles). We note that in general the GS follows similar trends as those observed by the entire MaNGA sample. In Figure 1, the GS shows a bimodality in the redshift-M_* plane and an increment of $R_{\rm eff}$ as M_* increases. It is also clear the cut on redshift from the GS is due to our selection criteria. In the inset of the bottom panel of Figure 1 we compare the spatial coverage of the GS with respect to its parent sample. The GS follows the distribution of the MaNGA sample. However, given our constrains to have both a reliable spatial coverage and good spatial sampling, its size is heavily reduced in comparison to the total sample of the MaNGA survey. In § 6 we explore the impact of deriving the azimuthal-averaged radial distributions using the entire low-inclined MaNGA sample.

2.3. pyPipe3D: *The Data-Analysis Pipeline*

To analyze the large amount of datacubes provided from the MaNGA survey we use the pyPipe3D analysis pipeline (Lacerda et al. 2022). This is an update in python language of the Fit3D and Pipe3D software and analysis pipeline (Sánchez et al. 2015, 2016) with significant improvements. Here we highlight the main features of this pipeline, while in Sanchez et al. (submitted) we provide a detailed description of the use of this pipeline for the entire MaNGA dataset.

In a nutshell, the pyPipe3D analysis pipeline disentangles the contributions of the stars and the ionized gas emission in the observed spectrum for each spaxel for each datacube. To obtain the contribution from the stellar component, the pipeline provides the best fit of the continuum using a linear combination of single-stellar populations (SSPs) spectra. To account for the line-of-sight velocity distribution function (LOSVD) first and second moments (i.e., the systemic stellar velocity, $V_{\rm los}$, and the stellar velocity dispersion, σ) the set of SSPs is shifted and convolved with a Gaussian function, as well as dust attenuated, adopting a Cardelli extinction curve (Cardelli et al. 1989). Details on how pyPipe3D estimates $V_{\rm los}$ and σ are described in Sánchez et al. (2015, 2016). The decomposition of the stellar continuum in different SSPs of a spectrum provides fundamental parameters of the stellar component. Thus, for each datacube pyPipe3D provides two-dimensional distributions (or maps) of the derived properties as well as their uncertainties. Among the many properties derived from the stellar continuum (see § 5 in Sanchez et al., submitted), we use in this study the maps of the following properties: the mass-to-light ratio (M/L), stellar mass density (Σ_*), the luminosity-weighted stellar age and metallicity (Age, [Z/H]), the dust attenuation ($\rm Av_{SSP}$), and the systemic stellar velocity ($V_{\rm los}$) and velocity dispersion (σ). Once the stellar continuum has been modeled by the SSPs for each datacube, it is removed from the observed datacube. This continuum-free datacube is thus used to estimate the properties from the emission lines. pyPipe3D pipeline provides a moment analysis to derive the physical properties for a large set of emission lines. For each emission line, the pipeline provides the map of its integrated flux, its systemic velocity, its velocity dispersion, and its equivalent width. We use these properties to build the radial profiles presented in this study for both the stellar and the ionized gas components.

2.4. *Radial Profiles and Gradients*

From the two-dimensional map of each galaxy's parameter derived by pyPipe3D we build its azimuthal-average radial profile. This procedure is performed for the entire MaNGA survey. For each map in each galaxy we make radial bins of 0.15 $R_{\rm eff}$ width up to $\approx$3 $R_{\rm eff}$. Projected in the sky each of these bins is an elliptical annulus centered on the optical (V-band) brightest region, with an ellipticity and position angle drawn from the NSA survey (Blanton et al. 2011). In Figure 3 we plot as example the radial distribution of the stellar mass surface density, Σ_*, for the MaNGA GS. Instead of plotting the radial gradients for individual galaxies, we plot for each morphological type (each panel in Figure 3) the median radial distribution for different bins of total stellar mass (each shaded area colored in Figure 3). The borders of those shaded areas show the 1-σ distribution for each galactocentric distance. To ensure a reliable estimation of the radial gradient we select those radial bins with good signal-to-noise ratio in the continuum (SNR $>$ 3) for stellar-derived properties, whereas for the emission-line-derived measurements, besides using a SNR cut in the continuum, we also impose a SNR cut in the Hα line (SNR $>$ 2). Furthermore, when calculating the median value for each morphology - stellar mass bin we exclude those radial bins where there are less than ten measurements.

As in other studies exploring the radial profiles of galaxy's properties (e.g., Sánchez-Menguiano et al. 2018), we note that a single-slope gradient for a large fraction of radial distributions is not accurate to describe them. In other words, to provide a proper description on how the physical properties of galaxies change at different galactocentric distances, it is required to use a procedure that fits more than one gradient. To account for these different variations in slopes we fit those radial distributions with a two-piece function. We fit the following functional form for a given radial profile $P(r)$:

$$P(r)=\begin{cases} P_0 + k_0(r/R_{\rm eff}), & r/R_{\rm eff} \leq r_0; \\ P_{\rm ini} + k_1(r - r_0/R_{\rm eff}), & r_0 \leq r/R_{eff} \leq r_1; \\ P_{\rm med} + k_2(r - r_1/R_{\rm eff}), & r_1 \leq r/R_{\rm eff}; \end{cases} \quad (1)$$

where $P_{\rm ini} = P_0 + k_0(r_0/R_{\rm eff})$ and $P_{\rm med} = P_{\rm ini} + k_1(r_1 - r_0/R_{\rm eff})$. The solid lines in Figure 3 represent the best fit of equation 1 for each radial distribution of Σ_*. Although we intended to constrain this fit to the typical size of the IFU ($\approx r/R_{\rm eff} < 2.5$), the piece-wise analysis provided an $r_0/R_{\rm eff}$ larger than 2.5. In turn, this suggests that the entire radial profile is well described by a single slope. It is evident that this functional form provides an accurate representation of the radial distribution for each morphology and stellar mass bin. In Appendix A we show the radial distribution, as well as the best-fit gradients, using equation 1 for the set of parameters explored using the MaNGA GS.

In the next sections (§ 3 and § 4), we present the best-fit parameters using equation 1 (i.e., the slopes of each line: k_0, k_1, k_2, and the break radius: r_0,

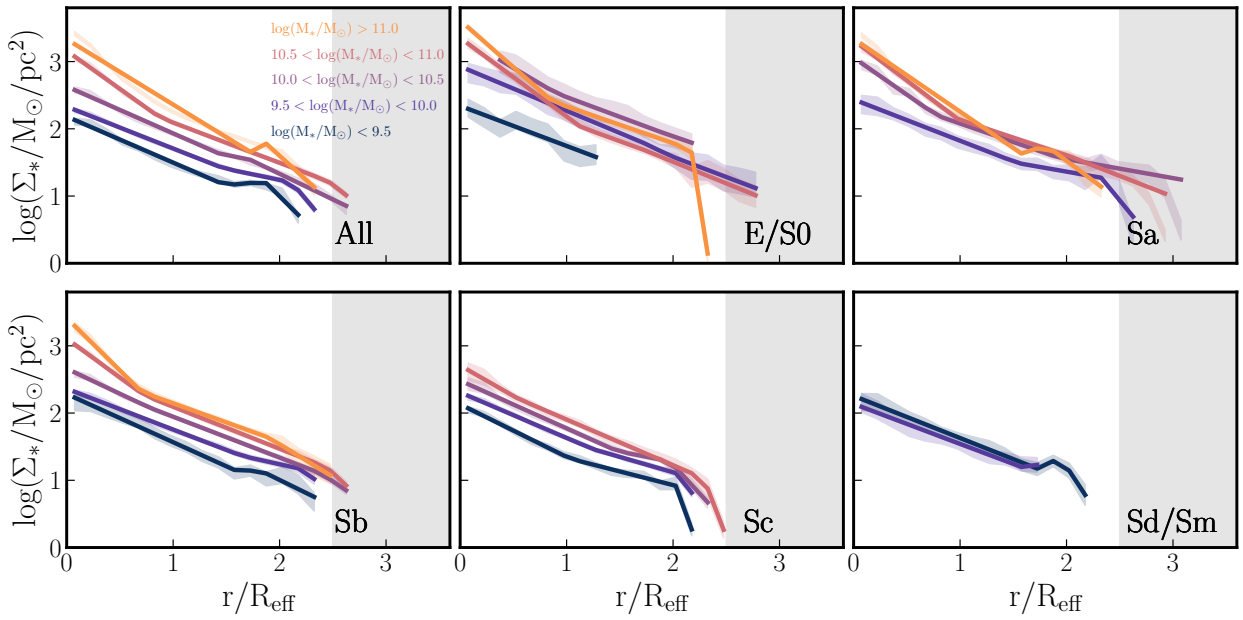

Fig. 3. The average radial distribution of the stellar mass density, Σ_*, as an example of the radial distribution of the physical properties derived for the GS of the MaNGA sample. The gradients are averaged by morphology (panels from left to right and top to bottom) and total stellar mass bins (shaded colored areas; each color represents a stellar mass bin see the legend in the top-left panel). The gray shaded area in each panel represent the typical maximum radius covered by the FoV ($R_{eff} \approx 2.5$). The solid lines in each panel represent the best fit derived from fitting a piecewise function to the radial distribution (see details in § 2.4). The color figure can be viewed online.

r_1), the differences between these slopes (Δ slope), and the value of each parameter at $R_{\rm eff}$. For the slopes as well as for the values derived at $R_{\rm eff}$ we show the uncertainty derived from the best fit. In general we find that the trends presented below for k_0, and k_1 with respect to the stellar mass are reliable in the sense that the uncertainties of these parameters are small in comparison to those trends. On the other hand, we find significantly large uncertainties for the outermost slope k_2, suggesting that the trends with respect to the stellar mass are not reliable. To avoid spurious results, in the following analysis we exclude those slopes derived where the range in galactocentric distance is smaller than $r/R_{\rm eff} < 0.3$ (i.e., $r_0 < 0.3$, and $r_1 - r_0 < 0.3$). This criteria exclude those slopes where the radial range is comparable to the size of the MaNGA PSF. We show for each of these parameters the variation with morphology for the different stellar mass bins (see as example Figure 4). When required, we also consider the uncertainties of these parameters in describing the observed trends. In other words, we describe these trends taking into account the associated error for each bin of stellar mass and morphology.

3. STELLAR PROPERTIES

3.1. *The M/L Ratio, and Stellar Mass Surface Density, Σ_**

As we mention above, galaxies show in general a decreasing radial distribution of their surface brightness in the optical(e.g., de Vaucouleurs 1958; Sersic 1968; Freeman 1970; Kormendy 1977). These surface brightness profiles are correlated mainly with the amount of stars that produce the observed flux via the mass-to-light ratio, M/L (e.g., Portinari & Salucci 2010). In Figure 33 we plot the median values of the M/L ratio for different morphologies and stellar masses, whereas in Figure 4 we summarize the best-fit parameters derived from the piece-wise analysis. From this analysis we find that the central slope, k_0, has mostly negative values and decreases with the total stellar mass – with little variation with respect to the morphology. Except for the Sb type, our analysis is not able to detect a significant value of k_1. For Sb galaxies the best-fit values of k_1 are negative and increase with M_* (except for most massive galaxies). For the outermost parts of the galaxies, the gradient of the M/L ratio, k_2, varies depend-

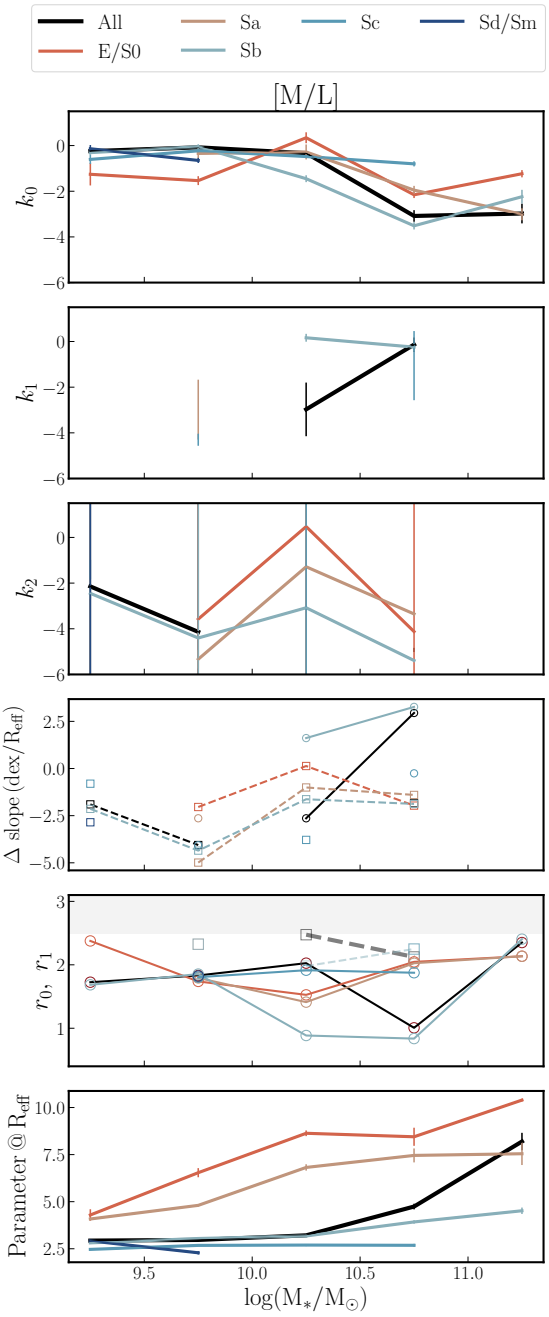

Fig. 4. Parameters derived from the radial distribution of the M/L ratio for different bins of total stellar mass. The color code of each symbol and line represents a morphological type (see legend). From top to bottom each panel shows: k_0, k_1, and k_2 from equation 1; the differences between those slopes (solid and dashed lines represent the $k_1 - k_0$, and $k_2 - k_0$ differences, respectively); r_0, and r_1 from equation 1 (solid and dashed lines, respectively); and the value of M/L at $R_{\rm eff}$. The color figure can be viewed online.

ing on both the stellar mass and morphology. For early-type galaxies with intermediate stellar mass, k_2 is positive or flat in comparison to the rest of mass-bins, where the slope is negative. For late-type galaxies k_2 is also negative with a more negative trend with M_* than k_0. These differences are highlighted in the fourth panel of Figure 4, suggesting a sharper drop of the M/L ratio in the outskirts of galaxies. We note a sharply negative slope for the most massive E/S0 galaxies bin (see top-middle panel in Figure 33). As this is a gradient derived with few data it is not reported in Figure 4. The fifth panel of Figure 4 indicates that those breaks of the gradients occur between ≈ 1.7 and 2.0 $R_{\rm eff}$. Finally, we note that for a given stellar mass bin, the M/L ratio at $R_{\rm eff}$ changes significantly for different morphologies. On average, late type galaxies present mild variations with M_* whereas early-type galaxies show significant variations of this ratio. This highlights the combined role of M_* and the morphology in shaping the radial distribution of the M/L ratio. These results reflect the different amount of old stars vs young stars for the different morphological types. Although less bright, old low-mass stars are the main contributor to the stellar mass in galaxies, at least for the mass and morphological ranges explored in this study.

One of the more significant parameters that represents a galaxy is its total stellar mass. Similarly, at spatially resolved scales, its local analog, the stellar mass surface density, Σ_*, has been observed to be a fundamental parameter to understand the angular distributions of different observables (e.g., Cano-Díaz et al. 2016; González Delgado et al. 2015; Sánchez 2020). In Figure 3 we show the average radial distributions of Σ_* for different masses and morphologies, as well as the gradients from the piecewise analysis. In Figure 5 we show the best-fit parameters from that analysis. We find similar distributions as those reported previously in the literature (e.g., González Delgado et al. 2015; Sánchez 2020). In general, regardless of the morphological type and the total stellar mass, Σ_* decreases with the galactocentric distance, with relatively similar slopes. The piece-wise analysis reveals that the slope for Σ_* at small galactocentric distances decreases from $k_0 \approx -0.5$ to $k_0 \approx -1.5$ dex/$R_{\rm eff}$, as M_* increases. We do not find a significant impact of morphology in setting the k_0 slope. The k_1 slope is rather stable for different masses and morphologies (except for low-mass galaxies where we find a flat gradient), although we note that it is not derived for low-mass or massive early-type galaxies, suggesting

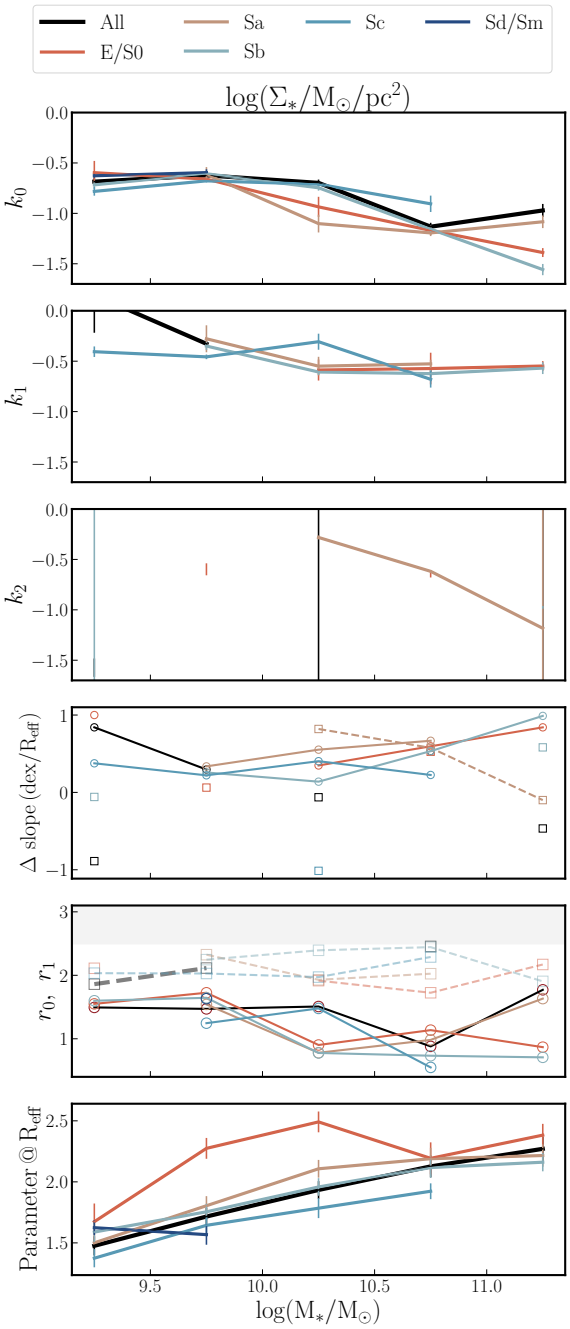

Fig. 5. Similar to Figure 4. Parameters derived from the piece-wise analysis for the stellar mass surface density gradients. The color figure can be viewed online.

that a single slope is required to estimate the gradient of these galaxies. Except for early-type galaxies, the analysis does not derive k_2 slopes, suggesting that for most bins of the M_*-morphology parameter space only a single or double slope is required to describe the Σ_* radial distribution. The difference between slopes suggest that in general the external gradient has a slightly more positive gradient than the inner one (i.e., $k_1 > k_0$). The break where the change of slope occurs is $r_0 \approx 0.5$ to 2.0 $R_{\rm eff}$, depending on the stellar mass and morphology. For those radial distributions with estimations of k_2, r_1 varies between 2.0 to 2.5 $R_{\rm eff}$. The characteristic value of Σ_* at $R_{\rm eff}$ increases with M_* with little effect from the morphology (except for early-type E/S0 galaxies where the characteristic value of Σ_* is larger in comparison to other morphologies).

3.2. *Luminosity Weighted Age, Metallicity, and Extinction*

Other than Σ_*, the SSP analysis also provides estimations of the average stellar age and metallicity, [Z/H]. In Figure 6 we show the parameters derived from the piece-wise analysis of the radial distribution of the luminosity-weighted stellar age (see Figure 34). The slope of the central gradient is in general negative ($k_0 \approx -0.3$ dex/$R_{\rm eff}$, although there are some stellar mass bins that exhibit an almost flat gradient, e.g., E/S0 low mass galaxies). When considering the morphology, this slope appears to decrease for late-type galaxies, while early-type galaxies tend to have either flat or mildly positive gradients. On average, the k_1 slope is slightly flatter than k_0, while the outer gradient (k_2) has a significantly larger negative value than the central gradient. For this analysis we exclude the sharp drops observed for k_2 in Figure 34, as those slopes are spurious. The radii where the change of slope occurs are relatively well confined ($r_0 \approx 1.0$ - 1.5 $R_{\rm eff}$, and $r_1 \approx 2$ $R_{\rm eff}$). By exploring the average stellar age at $R_{\rm eff}$, we find that early-type galaxies show the oldest ages in comparison to other morphological types. Furthermore, the stellar age measured at $R_{\rm eff}$ increases with M_* (black solid line in bottom panel of Figure 34). However, morphology may play a more significant role: late-type galaxies are in general younger than early-type ones. These results are in agreement with different studies presented in the literature (e.g., Sánchez-Blázquez et al. 2014a,b; González Delgado et al. 2015; Morelli et al. 2015; Zheng et al. 2017; Parikh et al. 2021). In order to describe these mild negative gradients, these studies suggest a 'inside-out' growth of the galaxies. We note that contrary to these studies, Goddard et al. (2017) found positive mass-weighted stellar age gradients for early-type galaxies (using the same dataset as this study), suggesting that an 'outside-in' growth for these galaxies. In this study, we find that in general, the age gradients are – mildly – negative, regardless the morphological type suggesting

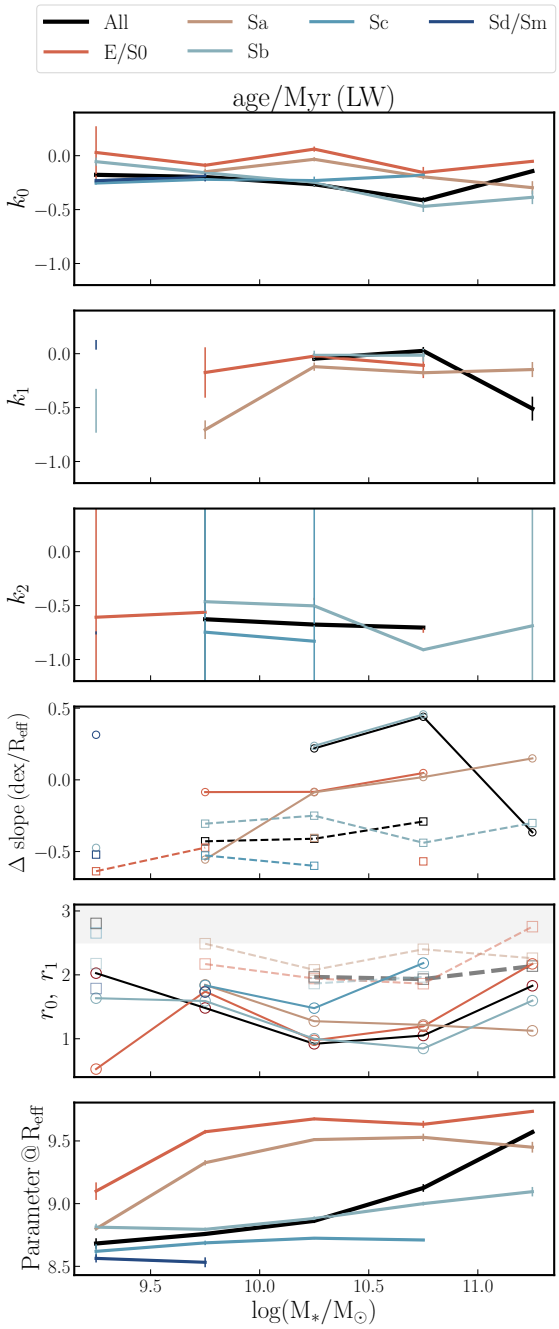

Fig. 6. Similar to Figure 4. Parameters derived from the piece-wise analysis for the luminosity-weighted age of the stellar population. The color figure can be viewed online.

an 'inside-out' growth for all the different morphological types or stellar masses.

In Figure 7 we show the result of the piece-wise analysis for the stellar metallicity radial profiles for our MaNGA GS (see Figure 35). We find that regardless of the morphology (except for intermediate-mass early-type galaxies), the gradient of the central radial profile (k_0) slightly decreases with M_*. For low-mass galaxies, this gradient is nearly flat, whereas most massive galaxies have a mild negative gradient ($k_0 \approx -0.1$ dex/$R_{\rm eff}$). Similar results have been found in the literature assuming a single gradient for the entire radial distribution of metals (e.g., S20). The slopes of the central gradients have been usually interpreted as an inside-out growth, more evident in massive galaxies. However, those galaxies where we are able to measure an external metallicity gradient (k_1, and k_2), usually have a flatter behavior than k_0. Even more, in some cases (e.g., Sb-Sc galaxies), we detect positive gradients, suggesting a radical change: an increment of metallicity at the outskirts of these galaxies. Since the gradients of the stellar metallicity have been usually described with a single negative slope (e.g., González Delgado et al. 2015; Zheng et al. 2017; Sánchez 2020), this could be an artifact due to either the lack of statistics at large galactocentric distances (although as we will explore in § 6, these trends are also observed when using a much larger sample) and/or the low signal-to-noise from the spectra at the outskirts of galaxies. Finally, we note that contrary to the stellar age at $R_{\rm eff}$, [Z/H] at $R_{\rm eff}$ depends significantly on M_* rather than on the morphology. The metallicity of the stellar component at this radius increases with M_*. Similar results have been found using the same dataset (Zheng et al. 2017).

From the stellar continuum fitting, the SSP analysis also allows us to have an estimation of the optical extinction afecting the stellar continuum, $\mathrm{Av_{SSP}}$. In Figure 8 we show the results of the piece-wise analysis to the radial distribution of $\mathrm{Av_{SSP}}$ (see Figure 36). From the piece-wise analysis we note that in the central portion of the galaxies the radial distribution of $\mathrm{Av_{SSP}}$ is almost flat with mild negative gradients for most morphological types ($k_0 \approx -0.1$ dex/$R_{\rm eff}$), except for early-type galaxies where these gradients are slightly positive. On the other hand, k_1 values change their sign, exhibiting a slight increment of $\mathrm{Av_{SSP}}$ as the galactocentric distance increases. For those sub-samples where we are able to measure k_2, we find stark drops in the values of $\mathrm{Av_{SSP}}$ as the galactocentric distance increases. Similar radial trends have been described in the literature using different IFU dataset (e.g., González Delgado et al. 2015). From the measurement of $\mathrm{Av_{SSP}}$ at $R_{\rm eff}$ we note that the absolute values are rather small ($\mathrm{Av_{SSP}} < 0.3$ mag). Contrary to other stellar properties derived from the SSP analysis, for the radial

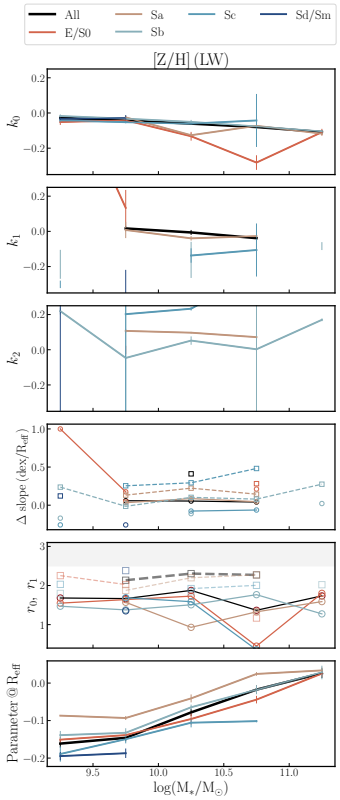

Fig. 7. Similar to Figure 4. Parameters derived from the piece-wise analysis for the luminosity-weighted stellar metallicity. The color figure can be viewed online.

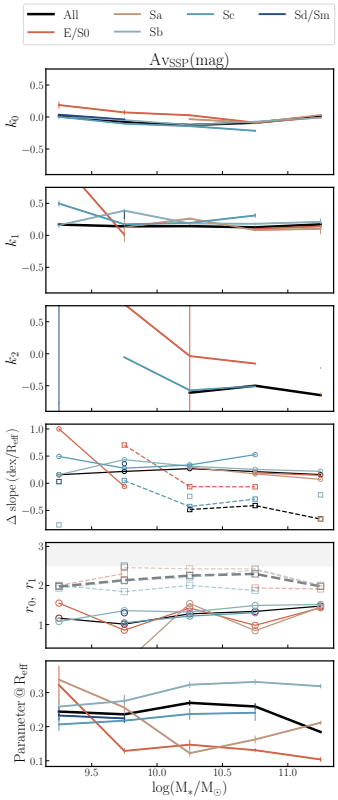

Fig. 8. Similar to Figure 4. Parameters derived from the piece-wise analysis for the optical extinction derived from the SSP analysis. The color figure can be viewed online.

distribution of the optical extinction it is not clear to disentangle the impact of either the morphology or M_*. Our analysis suggests that both structural parameters play a similar role in shaping the radial distribution of Av_{SSP}. In § 4.2.1 we show the ratio between Av_{SSP} and the optical extinction derived from the Balmer decrement.

4. EMISSION LINES PROPERTIES

As we mention in § 2.3, the pyPipe3D analysis pipeline provides the angular distribution of the properties of different emission lines observed in the optical (i.e., the integrated flux, equivalent width, velocity, and velocity dispersion) for each of the galaxies included in the MaNGA survey. These properties, including their ratios, has been widely used to explore physical properties of the ionized gas component of the ISM. In this section we explore the radial distribution of the properties derived directly by the pipeline (§ 4.1), and those derived from the flux ratios of these emission lines (§ 4.2, § 4.3, § 4.4, and § 4.5).

4.1. *Fluxes, and Equivalent Widths*

In Figure 9 we show the results of the piece-wise analysis for the four brightest emission lines in the optical regime: Hα, Hβ, [NII], and [OIII][9] (see their radial profiles in Figures 37, 38, 39, and 40). We first note that due to our SNR selection criteria, in particular the one from the Hα emission line, there are some bins of morphology/M_* where it is not possible to derive the gradients from these emission lines. This is the case for low-mass early-type (Sa) galaxies.

For those stellar masses and morphologies where we measure a gradient, the slope in the central region ($r < 1.5\ R_{\rm eff}$) is negative regardless of the emission line ($-1 < k_0 < 0$). For the Balmer emission lines, Hα and Hβ, we find little dependence of k_0 with respect to M_*. For late-type galaxies, $k_0 \approx -0.5$ dex/$R_{\rm eff}$. On the other hand, for early-type galaxies k_0 tends to be stepper in comparison

[9] Apart from these emission lines, the pyPipe3D analysis pipeline also allows us to derive the flux from low-brightness emission lines.

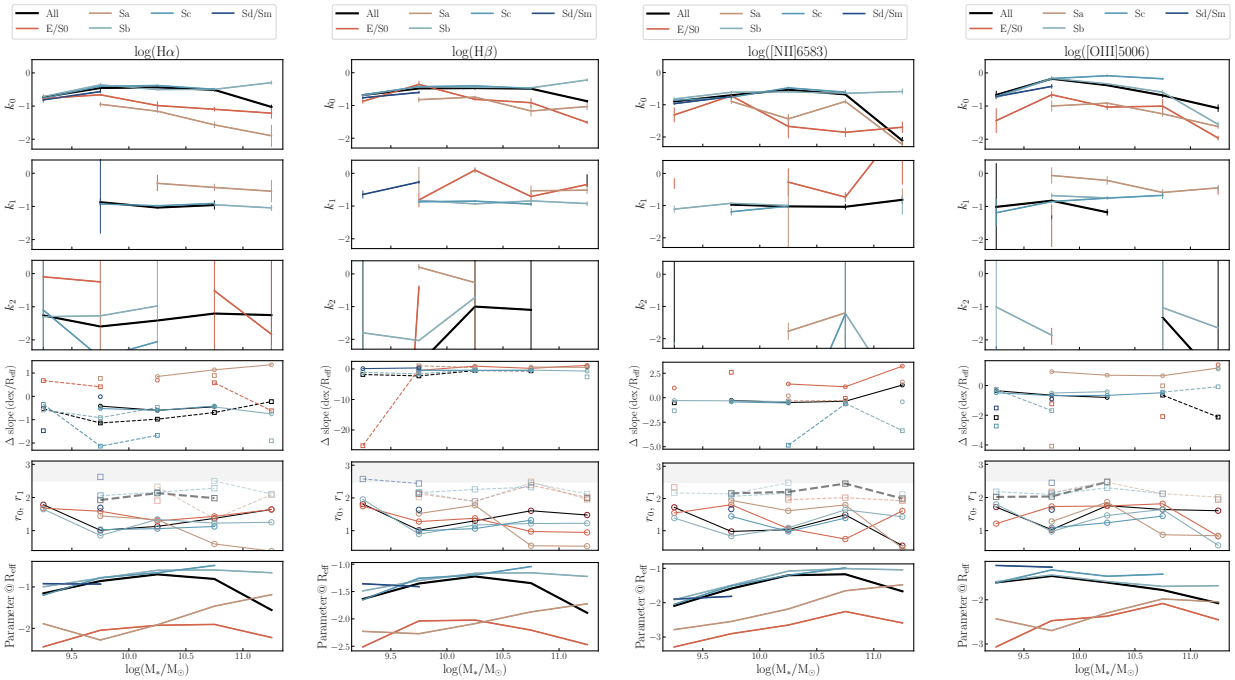

Fig. 9. Parameters derived from the piece-wise analysis for the four brightest emission lines in the optical. From left to right: Hα, Hβ, [NII], and [OIII]. The color figure can be viewed online.

to that derived for late type ones at the same stellar mass bin. For those galaxies where we are able to estimate an external gradient (k_1), we find, in general, steeper negative gradients in comparison to k_0 for late-type galaxies, whereas for early galaxies $k_1 > k_0$. For the [NII] emission line k_0 slightly increases with M_* , reaching a constant value of $k_0 \approx -0.5$ dex/$R_{\rm eff}$ (except for the most massive bin where k_0 is significantly steeper, $k_0 \approx -2$ dex/$R_{\rm eff}$). Similar to the Balmer lines, the slope of the central gradient for the [NII] lines for early-type galaxies is steeper in comparison to late-type galaxies for the same stellar mass bin. For this emission line the outer gradients are steeper than those derived in central regions. On the other hand, for the [OIII] emission line we find that the central gradient, k_0, decreases with the stellar mass: low-mass galaxies have a flatter gradient in comparison to massive ones. Similar to the other emission lines, we estimate negative steeper gradients for the outskirts of galaxies (k_1). The sharp drop of the gradients at the outskirts for the different emission lines could be expected given the low signal-to-noise from these lines at those large galactocentric radii. For the Hα, Hβ, and [NII] emission lines their fluxes at $R_{\rm eff}$ slightly increase with the stellar mass. For early-type galaxies the flux of these emission lines at $R_{\rm eff}$ is significantly fainter than that derived for late-type galaxies. On the other hand, the flux of the [OIII] slightly decreases with the stellar mass.

The equivalent width of the Hα emission line, EW(Hα), has been extensively used to explore the star-formation activity of galaxies at both integrated and spatially resolved scales (e.g., Sánchez et al. 2012; Lacerda et al. 2018). Therefore, it is quite relevant to understand how this parameter changes with radius. In Figure 10 we present the piece-wise analysis of the radial distribution for the EW(Hα). The radial distributions of EW(Hα) for different bins of stellar mass and morphology are presented in Figure 41. We find that the slope of the central gradient of EW(Hα) is nearly constant for different bins of M_* , regardless of morphology. However, we note that although late-type galaxies show a positive gradient, early-type galaxies show a nearly flat gradient. Interestingly, we find a change in the slope of the radial distribution of EW(Hα) for the outskirts of late-type galaxies (i.e., k_1, and k_2 are negative). This change in the slope occurs at ≈1.0 - 1.5 $R_{\rm eff}$. This may reflect the impact of morphological features on setting the radial distribution of the EW(Hα) in these galaxies. Finally, when we explore the value of EW(Hα) at $R_{\rm eff}$, we find that low-mass late-type galaxies (Sd/Sm) have the largest values of EW(Hα). For the other late-type morphological bins we note that as M_* increases the value of EW(Hα) at $R_{\rm eff}$

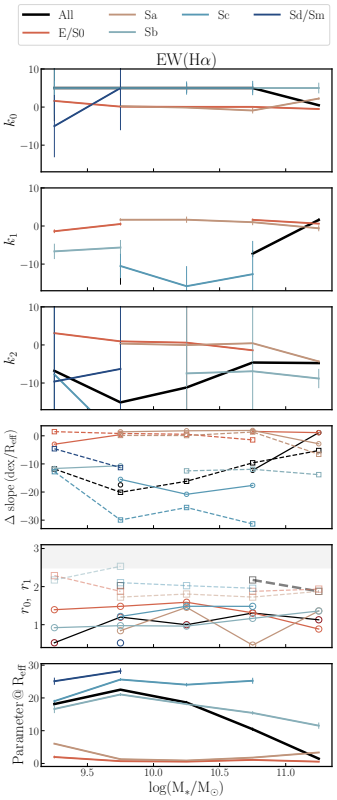

Fig. 10. Parameters derived from the piece-wise analysis for the Hα emission line equivalent width. The layout of the figure is similar to Figure 4. The color figure can be viewed online.

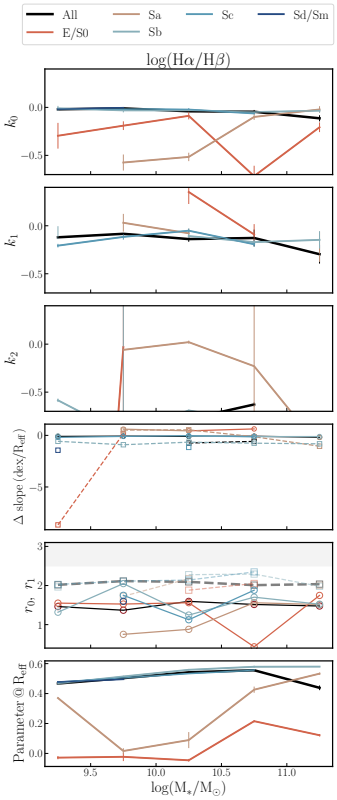

Fig. 11. Parameters derived from the piece-wise analysis for the Balmer decrement. The layout of the figure is similar to Figure 4. The dashed lines represent the expected value of this ratio from a Case B of recombination (Hα/Hβ= 2.86). The color figure can be viewed online.

tends to decrease. On the other hand, for early-type galaxies, the EW(Hα) measured at $R_{\rm eff}$ is constant regardless M_* (EW(Hα) $<$ 6 Å). This value has been used to differentiate star-forming regions from other ionization mechanisms (e.g., Cid Fernandes et al. 2011; Lacerda et al. 2018, see dashed line in Figure 41). As derived in other studies, we find that the star-formation activity is largely affected by the morphology rather than by the stellar mass (e.g., Sánchez 2020, and references therein).

4.2. *Line Ratios*

The ratios between fluxes of different emission lines have been essential to explore physical properties of the ISM. In this section we describe the radial gradients and the best-fit gradients of three emission-line ratios from the brightest lines presented in the previous section (Hα, Hβ, [NII], and [OIII]).

4.2.1. *Balmer Decrement,* Av$_{\rm gas}$ *, and* $\Sigma_{\rm mol,Av}$

The Hα/Hβ flux lines ratio (also known as the Balmer decrement, BD) has been extensively used to estimate the effect of the dust on the optical extinction (Av$_{\rm gas}$; e.g., Kennicutt 1992; Brinchmann et al. 2004; Moustakas et al. 2006; Domínguez et al. 2013). Recently, in Barrera-Ballesteros et al. (2020) we provided a proxy between Av$_{\rm gas}$ and the molecular gas surface mass density, $\Sigma_{\rm mol}$, at kpc scales using the spatially resolved data from the optical and the molecular gas of the EDGE-CALIFA survey.

In Figure 11 we present the piece-wise analysis of the Hα/Hβ radial profiles for our MaNGA Golden Sample, whereas in Figure 42 we show the radial distribution of the BD as well as the best-fit gradients derived from this analysis. In Figure 42 we also indicate the theoretical value of this ratio $\approx$ 2.86 (see dashed lines; this is the expected value for the Hα/Hβ ratio for a temperature of 10^4 K and Case B of recombination, Osterbrock & Ferland 2006; Raga et al. 2015). From the piece-wise analysis we find that the central gradient (k_0) for late-type galaxies is rather constant and flat for different stellar mass bins (i.e., $k_0 \approx 0$ dex/$R_{\rm eff}$). For the early-type galaxies

the central gradients vary significantly between negative and flat for the different bins of probed stellar mass. For those galaxies where we are able to estimate external gradients (i.e., k_1 and k_2) we find that these are mostly negative. The values of the Balmer decrement measured at $R_{\rm eff}$ show that this parameter increases with M_* for late-type galaxies. Furthermore, we find that for all late-type galaxies – at least within 1 $R_{\rm eff}$ – the BD is larger than the expected value from theory (see dashed line in Figure 11). On the other hand, only the most massive Sa galaxies have a BD larger than 2.86. For the rest of the early-type galaxies the BD measured at $R_{\rm eff}$ is smaller than this value. Furthermore we note that for E/S0 galaxies BD ≈ 1, suggesting that the flux from these two lines is close to the values expected from fluctuations within the noise. The fact that for most of the late-type galaxies, regardless of the stellar mass, the BD distribution is larger than 2.86 suggests that it is possible to have a radial measurement of the optical extinction from this ratio. On the other hand, for early-type galaxies it is not possible to estimate the optical extinction from the Hα/Hβ ratio since their values are smaller than the one expected from the case B of recombination.

We follow Barrera-Ballesteros et al. (2020) and Catalán-Torrecilla et al. (2015) to estimate the optical extinction for the Hα emission line, A(Hα). Assuming a Cardelli extintion curve with $R_V = 3.1$ (Cardelli et al. 1989), the optical extinction is given by:

$$\mathrm{Av_{gas}} = A(\mathrm{H}\alpha)/0.817. \quad (2)$$

Thus to estimate $\mathrm{Av_{gas}}$ we do not consider those radial bins in galaxies where BD < 2.86. In Figure 12 we present the result of the piece-wise analysis of the radial distribution of $\mathrm{Av_{gas}}$ (see Figure 43). As in the previous analysis, for early-type galaxies it is not possible to derive $\mathrm{Av_{gas}}$ from the Balmer decrement because most of the radial bins have a value of the BD smaller than 2.86. Therefore, most of the results presented in Figure 12 are for late-type galaxies, in particular Sb, and Sc ones. For a wide range of stellar masses (i.e., $9.2 < \log(M_*/M_\odot < 10.7$), the gradient of $\mathrm{Av_{gas}}$, k_0, decreases with M_* (from $k_0 \approx -0.2$ mag/$R_{\rm eff}$ to $k_0 \approx -0.4$ mag/$R_{\rm eff}$). For the most massive bin, the gradients are flatter. The radial extension of $\mathrm{Av_{gas}}$ goes up to ≈ 1.5 $R_{\rm eff}$. When measuring $\mathrm{Av_{gas}}$ at $R_{\rm eff}$, we find that this extinction increases with M_*. For low-mass galaxies $\mathrm{Av_{gas}} \approx 0.2$ mag, whereas massive ones show values of $\mathrm{Av_{gas}} \approx 1.0$ mag. Our results show the impact that M_* has in setting the radial distribution

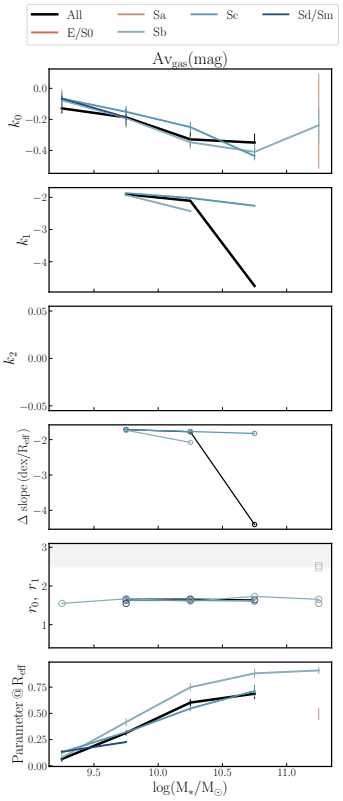

Fig. 12. Parameters derived from the piece-wise analysis for the optical extinction derived from the Balmer decrement, $\mathrm{Av_{gas}}$. The layout of the figure is similar to Figure 4. The color figure can be viewed online.

of $\mathrm{Av_{gas}}$ in late-type galaxies: the more massive is the galaxy the steeper is the gradient of $\mathrm{Av_{gas}}$.

Since we have the estimation of the optical extinction from both the stellar continuum ($\mathrm{Av_{SSP}}$) and the emission lines ($\mathrm{Av_{gas}}$) we are able to compare the radial variations of the ratio of these values. Different studies have explored this ratio for integrated and angular resolved scales. On the one hand, some studies suggested that this ratio is constant for late-type galaxies in both integrated and spatially-resolved measurements (e.g., Calzetti 1997; Calzetti et al. 2000; Kreckel et al. 2013). On the other hand, other studies have suggested variations of this ratio for different local and global properties (e.g., Wild et al. 2011; Koyama et al. 2015, 2019; Qin et al. 2019; Lin & Kong 2020; Li et al. 2021).

In Figure 13 we present the results of the piece-wise analysis of the radial distribution of the $\mathrm{Av_{gas}}/\mathrm{Av_{SSP}}$ ratio (see Figure 44). We first note that the ratio of these two estimations of the optical extinction is not constant with radius. Furthermore the gradient of this ratio varies depending on the

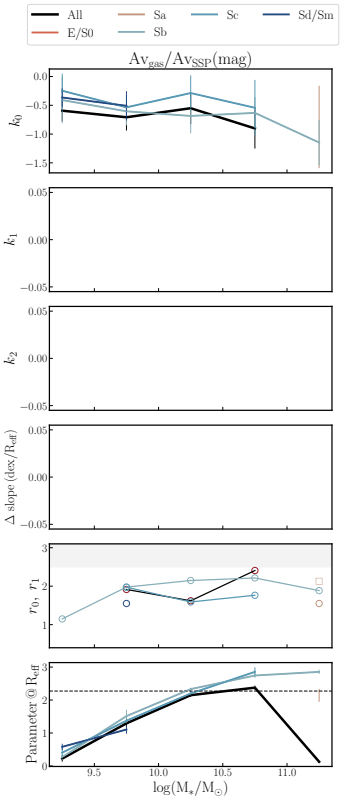

Fig. 13. Parameters derived from the piece-wise analysis for the Av_{gas} /Av_{SSP} ratio. The layout of the figure is similar to Figure 4. The dashed line in the bottom panel shows the value derived from Calzetti (1997): Av_{gas} /$Av_{SSP} \approx 2.27$. The color figure can be viewed online.

stellar mass. As for Av_{gas}, the radial extension of this ratio is limited by the Hα SNR selection criteria. Therefore, for most radial distributions, a single gradient (k_0) describes well the entire radial distribution. Also similar to Av_{gas}, this ratio is derived mostly for late-type galaxies. We find a similar trend in k_0 as the one described by Av_{gas} with respect to the stellar mass. The gradient of this ratio decreases with M_*; massive galaxies have steeper negative gradients in comparison to low-mass ones. The value of this ratio at $R_{\rm eff}$, increases with M_*; going from values below 1 to 3 from low-mass to massive galaxies, respectively. The bottom panel of Figure 13 shows that only intermediate mass Sb galaxies have a similar ratio as the one expected in the literature (Calzetti 1997). Our results suggest that the estimation of the optical extinction varies depending on the adopted proxy (i.e., ionized gas or stellar). Furthermore, this ratio shows a significant variation radially, as well as with the stellar mass. In contrast to studies that proposed a constant stellar-gas extinction ratio (Calzetti 1997; Calzetti et al. 2000; Kreckel et al. 2013), we find significant variations of this ratio across the optical extension of the probed galaxies. Different studies have suggested that a possible scenario to explain these differences is due mainly to geometrical effects (e.g., Price et al. 2014; Reddy et al. 2015; Koyama et al. 2019). Nevertheless, using a sample of galaxies also included in the MaNGA survey, Lin & Kong (2020) and Li et al. (2021) found that the difference in this ratio is due to different properties from both the stellar and the ionized gas components. On the one hand, Lin & Kong (2020) found that this ratio strongly depends on the oxygen abundance as well as on the ionization stage at kpc scales. On the other hand, Li et al. (2021) found that this ratio also depends on the luminosity-weigthed age, thus the Av_{gas} /Av_{SSP} ratio. Therefore, our results favor the scenario presented by these works where the extinction (i.e., the dust properties) is affected (mainly) by local physical conditions, such as the chemical enrichment of the ISM and/or the ionization parameter.

As we mention above, using a sample of galaxies with spatially resolved observations of the molecular gas and the optical properties we estimate a calibrator between the optical extinction derived from the Balmer decrement (Av_{gas}), and the molecular gas surface density, $\Sigma_{\rm mol}$ (Barrera-Ballesteros et al. 2020). Using this calibration, we present in Figure 14 the piece-wise analysis of the radial distribution of the molecular gas density, $\Sigma_{\rm mol,Av}$, derived from the optical extinction, Av_{gas} (see radial profiles in Figure 45). As expected, we find similar trends of the gradients and values of $\Sigma_{\rm mol,Av}$ at $R_{\rm eff}$ with respect to the stellar mass and morphology in comparison to those derived for Av_{gas}. The gradient of $\Sigma_{\rm mol,Av}$ decreases with respect to M_* and is available in general only for late-type galaxies. However, we note that the gradients from $\Sigma_{\rm mol,Av}$ are flatter in comparison to those derived from Av_{gas}. The value of $\Sigma_{\rm mol,Av}$ at $R_{\rm eff}$ increases with the stellar mass. Following this calibrator as a reliable estimation of $\Sigma_{\rm mol}$ at kpc scales, our results suggest that, except for low-mass galaxies, the radial distribution of $\Sigma_{\rm mol}$ slightly decreases with radius.

Finally, given the estimation of $\Sigma_{\rm mol,Av}$, we can also provide a measurement of the ratio between the molecular and stellar gas surface mass density – $f_{\rm mol}$= $\Sigma_{\rm mol,Av}$ / Σ_*. In Figure 15 we show the piecewise analysis of the radial distribution of log($f_{\rm mol}$) (see Figure 46). We find that, in general, regardless of the stellar masses and morphologies probed, $f_{\rm mol}$

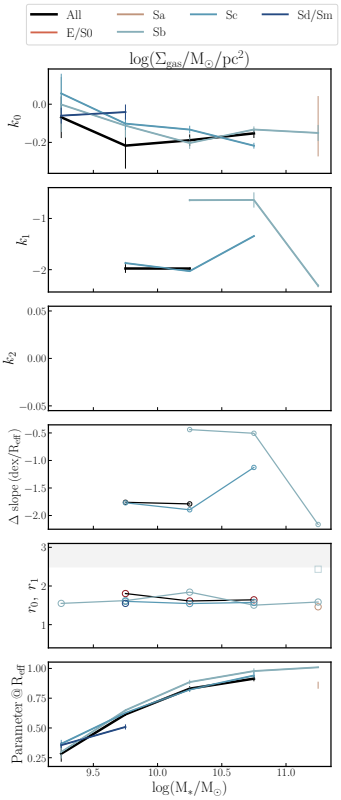

Fig. 14. Parameters derived from the piece-wise analysis for the molecular gas mass derived from $\mathrm{Av_{gas}}$, $\Sigma_{\mathrm{mol,Av}}$. The layout of the figure is similar to Figure 4. The color figure can be viewed online.

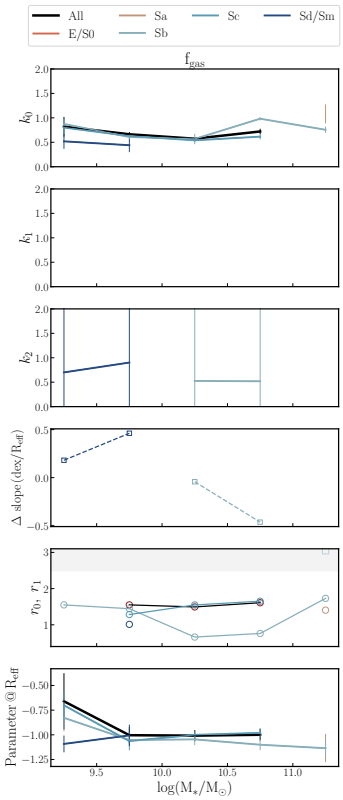

Fig. 15. Parameters derived from the piece-wise analysis for the gas fraction, $\mathrm{f_{mol}}$. The layout of the figure is similar to Figure 4. The color figure can be viewed online.

has a positive constant gradient ($k_0 \approx 0.7$ dex/R_{eff}). We also find that, except for the low mass galaxies, the gas fraction measured at the effective radius is relatively constant for the range of probed stellar masses with $\log(\mathrm{f_{mol}}) \approx -1.1$. Our results suggest that the gas density, with respect to the stellar mass density, increases at large radii. In other words, in comparison to the radial gradient of Σ_*, the radial distribution of $\Sigma_{\mathrm{mol,Av}}$ is rather flat. The small variations in both slope and $\mathrm{f_{mol}}$ at R_{eff} for different stellar masses suggest that this radial trend is an ubiquitous property for late-type galaxies.

4.2.2. *Other Line Ratios*

Apart from the Hα/Hβ ratio, there are other emission line ratios that provide insights on the physical condition of the ISM – and even on the very young stellar population – in galaxies. This is the case of the [NII]/Hα ratio. In star-forming galaxies, this ratio has been linked to the fraction of young stellar population (e.g., Sánchez et al. 2015). In Figure 16 we present the parameters derived from the piece-wise analysis from the radial distribution of this emission line ratio (see Figure 47). Except for E/S0 low-mass galaxies, we find that regardless of M_* , the central gradient (k_0) has negative values with a mild decrease with stellar mass. On the other hand, for early-type galaxies we find a change from positive to negative gradients as stellar mass increases. For the external part of the galaxies, we note that the piece-wise analysis yields positive gradients (in some cases sharp ones, e.g., Sb galaxies). We consider that those strong radial variations of the [NII]/Hα ratio at the outskirts of these galaxies could be spurious, induced by low SNR values of both emission lines. At low SNRs, emission lines fluxes tend to be similar to each other, in other words, the ratio is close to $\approx$ 1. The [NII]/Hα ratio measured at R_{eff} increases with M_* from $\log([\mathrm{NII}]/\mathrm{H}\alpha) \approx -0.8$ dex to $\log([\mathrm{NII}]/\mathrm{H}\alpha) \approx -0.2$ dex, for late-type galaxies. For early-type galaxies, this ratio measured at R_{eff} does not significantly changes with M_* , with a constant value of $\log([\mathrm{NII}]/\mathrm{H}\alpha) \approx -0.2$ dex.

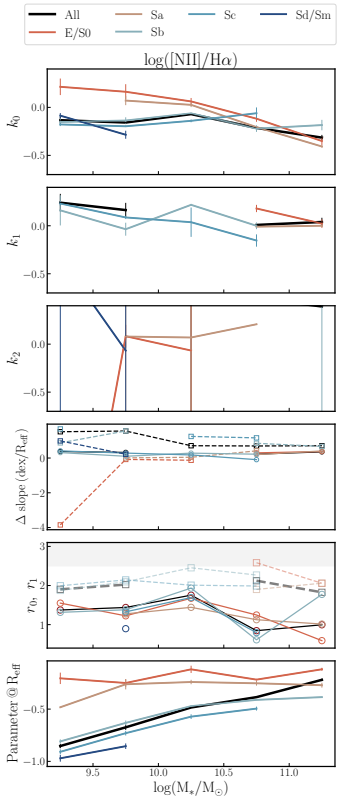

Fig. 16. Parameters derived from the piece-wise analysis for the [NII]/Hα emission lines ratio. The layout of the figure is similar to Figure 4. The color figure can be viewed online.

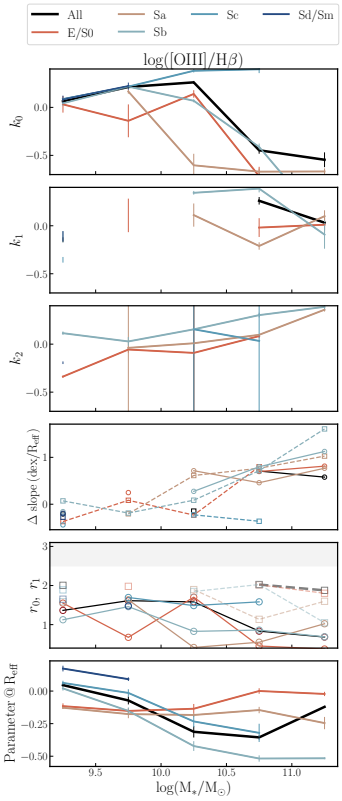

Fig. 17. Parameters derived from the piece-wise analysis for the [OIII]/Hβ emission lines ratio. The layout of the figure is similar to Figure 4. The color figure can be viewed online.

In Figure 17 we show the results of the piece-wise analysis for the radial distribution of the [OIII]/Hβ ratio (see Figure 48). The central gradient (k_0) of this ratio has significant variations for both different morphologies and stellar masses. On the one hand, for late-type galaxies k_0 is positive and increases from low to intermediate stellar masses. However, for massive galaxies k_0 is negative becoming larger (negative and stepper) as M_* increases. On the other hand, for early-type galaxies k_0 varies from positive to negative for different bins of stellar mass. In contrast to k_0, k_1 and k_2 have larger positive gradient indicating the strong radial variation of the [OIII]/Hβ ratio. Given the fact that these variations occur at smaller radius than the [NII]/Hα ratio (≈ 1 $R_{\rm eff}$, and ≈ 2 $R_{\rm eff}$, respectively), we suggest that these variations may have a physical origin. For instance, large central [OIII]/Hβ ratios could be indicating the presence of a hard ionizing source (e.g., an active nucleus), whereas large ratios at the outskirts could be due to ionization from a large star formation activity. Nevertheless, we cannot rule out that, as for the [NII]/Hα ratio, these variations in gradients are due to low SNR measurements. Contrary to the [NII]/Hα ratio, we find that both M_* and the morphology play a significant role in setting the observed [OIII]/Hβ ratio at $R_{\rm eff}$. For late-type galaxies, [OIII]/Hβ measured at $R_{\rm eff}$ decreases with M_*. However, for a given stellar mass bin, this ratio decreases from Sd/Sm to Sb galaxies. On the other hand, for early-type galaxies this ratio is rather constant for different bins of M_*. Furthermore, the value of this ratio is similar to the one derived from the [NII]/Hα ratio for this morphological type. In the next section, using these two line ratios, we explore the possible ionization mechanism that could explain their radial distribution.

4.2.3. *The BPT Diagram*

Diagnostic diagrams using emission-line ratios are very useful tools to probe the ionization stage of entire galaxies and kpc regions within them. Depending on the position of the galaxy/region in this diagram it can be associated with a different ioniza-

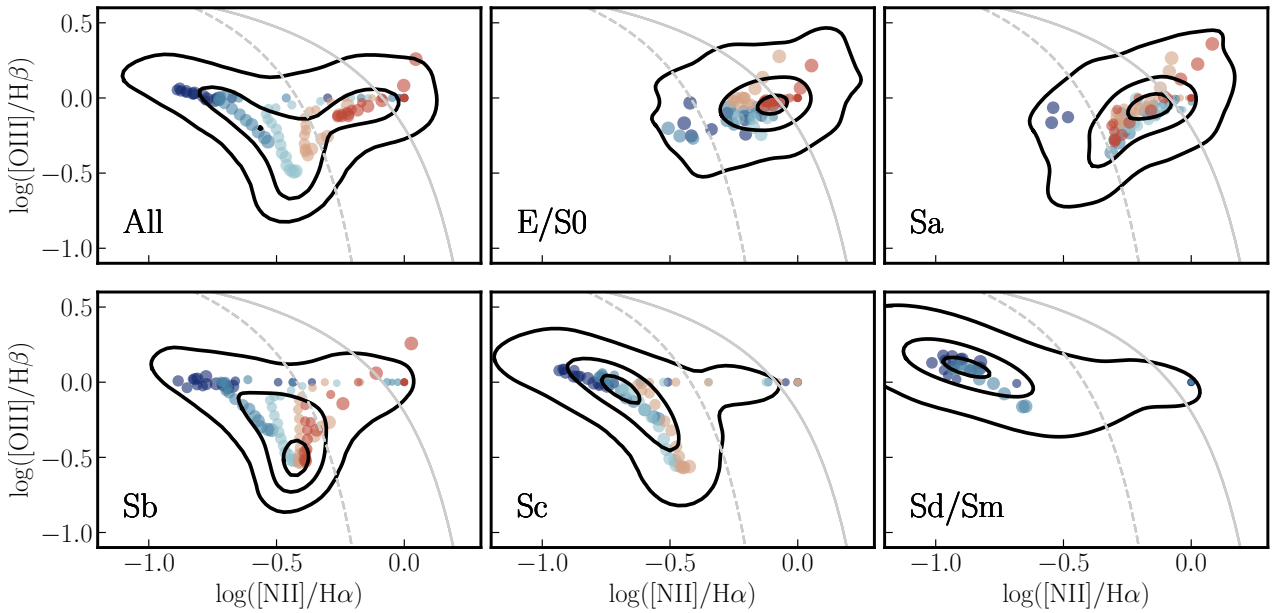

Fig. 18. The BPT diagnostic diagram using the radial averages for the Golden Sample. The contours enclose 90%, 50%, and 10% of the line ratios for the radial bins. In each panel we segregate the samples according to their morphology (see the label in each panel). The circles represent the averaged values for different bins of stellar mass. The color of each circle represents the stellar mass, following the same color code as in Figure 3. The sizes of the circles decrease with galactocentric distance. The solid and dashed gray lines represent the demarcation lines in this diagram by Kewley et al. (2001) and Kauffmann et al. (2003), respectively. The color figure can be viewed online.

tion process. The ionizing stage is segregated by the so-called demarcation lines. Prior to the large IFU surveys mapping, a large number of targets, galaxies with line ratios below the Kauffmann demarcation line (Kauffmann et al. 2003), were considered as star-forming, whereas galaxies above the Kewley demarcation line (Kewley et al. 2001) were considered as AGNs or LINERs. Galaxies in between were considered as 'composite', that is, a mixture between both types of ionization. This picture has significantly changed thanks to angular-resolved observations (for a review see Sánchez 2020; Sánchez et al. 2021). In Figure 18 we show the best known of those diagrams, the BPT diagram (Baldwin et al. 1981) for the ratios derived for the radial bins of the MaNGA GS. We find that the distribution of flux ratios varies depending on the morphology, the stellar mass, and the galactocentric distance. For the entire GS (top left panel in Figure 18), we find a significant difference between low-mass and massive galaxies. On the one hand, central regions of massive galaxies are above the Kewley et al. (2001) demarcation lines, suggesting that the ionizing source for those regions is dominated by processes other than star formation. Furthermore, as distance increases the flux ratios from massive galaxies move below the demarcation lines indicating that the ionization could be due to star formation. The massive galaxies follow what has been identified as the composite/AGN branch using single-fiber spectroscopy(e.g., Kauffmann et al. 2003, using SDSS dataset). On the other hand, as stellar mass decreases, most of the radial bins are below the Kauffmann demarcation line. This suggests that the ionization source for those galaxies, regardless of the galactocentric distance, is due to star formation. Furthermore, the lowest mass bin exhibits the lowest values of the [NII]/Hα ratio. The radial bins follow the star-formation branch observed using the SDSS dataset (e.g., Kauffmann et al. 2003).

For the E/S0 morphological bin (top-middle panel of Figure 18), the radial values of these emission line ratios (black contours) are mostly above the Kauffmann et al. (2003) demarcation line (gray-dashed line). Similar to the contours, these values are slightly below the Kewley et al. (2001) demarcation line. Although this could indicate that the ionization source could be due to an AGN (e.g., Husemann et al. 2010, 2014), this is only plausible in the central regions of these galaxies. It could also be that the ionization is due to hot-evolved stars (also known as HOLMES, e.g., Binette et al. 1994; Flores-Fajardo et al. 2011). To further constrain the

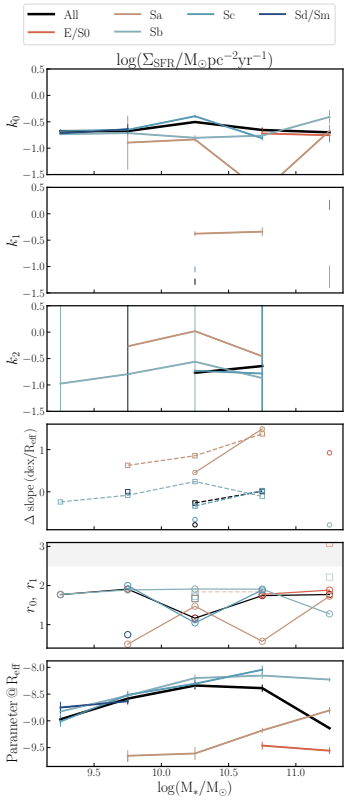

Fig. 19. Parameters derived from the piece-wise analysis for the radial distribution of the $\Sigma_{\rm SFR}$. The layout of the figure is similar to Figure 4. The color figure can be viewed online.

source that ionizes the ISM it has been also required to measure the EW(Hα) (e.g., Cid Fernandes et al. 2010, 2011; Barrera-Ballesteros et al. 2016; Lacerda et al. 2020). Similarly, Sánchez (2020) explored the distribution of the EW(Hα) for a large sample of IFS datasets at kpc scales within the BPT diagram for different stellar masses and morphologies. His results showed that indeed for massive E/S0 galaxies the distribution of the emission line ratios in the BPT diagram is between the Kauffman and Kewley demarcation lines, with EW(Hα) values smaller than 6Å (below this threshold it is expected that the ionization source is mainly due to HOLMES; e.g., Cid Fernandes et al. 2011). We should also note that most of the averaged values for different stellar mass bins at the outskirts of E/S0 galaxies (small circles of different colors) are located close to the region where both ratios are close to one. As we mention above, we cannot rule out that these positions of the flux ratios in the BPT diagram are simply due to measured fluxes with low SNR. For Sa galaxies the distribution of the flux ratios measured in their radial bins spreads wider across the BPT diagram than for E/S0 galaxies. Nevertheless, as we mention for E/S0 galaxies, the outer radial bins, regardless of M_* are mostly concentrated where the ratios are close to one. For the central radial bins of the most massive galaxies the ratios are well above the Kewley demarcation line, whereas the ratios from central regions in low-mass galaxies are well below the Kauffmann demarcation line. The Sb galaxies show a similar distribution as the entire sample, with low-mass galaxies lying below the Kauffmann demarcation line and massive galaxies spreading along the 'non star-forming' branch. The flux ratios from most of the radial bins of Sc galaxies lie below the Kauffmann demarcation line; furthermore, they lie in the so-called 'star-forming' branch. This suggests that for galaxies of this morphological type the ionization is due mostly to star formation across their optical extension, regardless of the stellar mass. For the irregular galaxies (Sd/Sm), we find that the [OIII]/Hβ ratio is rather constant for the probed galaxies ([OIII]/H$\beta \approx 1$). The [NII]/Hα ratio, on the other hand, covers a wider dynamical range than any other morphological type ($0.1 <$ [NII]/Hα < 3). For the irregular galaxies, we find flux ratios only for low-mass galaxies. In the BPT diagram, these ratios are located well below the Kauffmann demarcation line, suggesting that these ratios are the result of ionization due to star formation. Finally, we note that for those radial bins at the outskirts of galaxies both flux ratios tend to be close to one. We observe a similar behavior for the radial distribution of each line ratio (see § 4.2.2). Rather than indicating an ionization source other than star formation, this suggests that the low SNR from these emission lines at external radii do not allow us to derive their true ionization source.

4.3. *Star-Formation Parameters*

The Balmer emission lines are also a powerful tools to gauge the star formation rate (SFR) for galaxies/regions (Kennicutt & Evans 2012, and references therein). From the optical, following Kennicutt (1998), we can use the extinction-corrected luminosity of the Hα emission line as proxy of the star formation rate. This calibration has been widely used in IFS studies (e.g., Sánchez et al. 2012; Cano-Díaz et al. 2016, 2019). Apart from the SNR threshold for the Hα emission line, we did not use other selection criteria to derive the radial distribution of the SFR; thus, for some morphological types (e.g., E/S0) the radial profiles should be considered as upper limits of star formation. In this section we

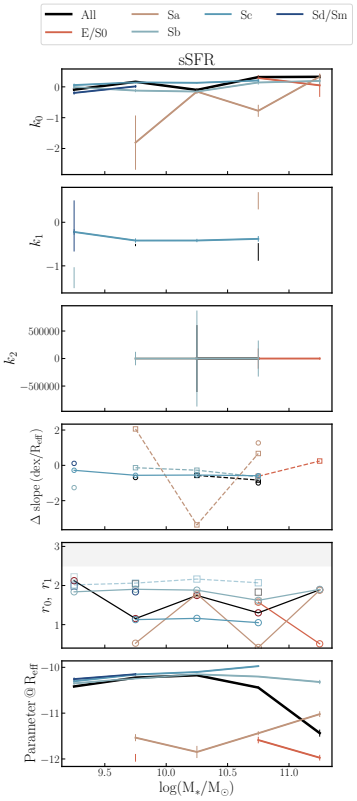

Fig. 20. Parameters derived from the piece-wise analysis for the radial distribution of the sSFR. The layout of the figure is similar to Figure 4. The color figure can be viewed online.

explore the radial distribution of the SFR density, $\Sigma_{\rm SFR}$, as well as its ratio, with the different components of the baryonic mass: the specific SFR, sSFR $= \Sigma_{\rm SFR}/\Sigma_*$; and the star formation efficiency, SFE $= \Sigma_{\rm SFR}/\Sigma_{\rm mol,Av}$. The radial distribution of these parameters is fundamental to understand what drives or halts the star-formation activity in galaxies (e.g., Colombo et al. 2020; Ellison et al. 2020).

4.3.1. *SFR Surface Density,* $\Sigma_{\rm SFR}$

In Figure 19 we plot the piece-wise analysis of the radial distribution of $\Sigma_{\rm SFR}$ (see Figure 49). We find that the central gradient of $\Sigma_{\rm SFR}$, k_0, is negative regardless of the stellar mass or morphology. Furthermore, k_0 is quite similar for the late-type galaxies regardless of M_* ($k_0 \approx -0.7$ dex/$R_{\rm eff}$). For the Sa galaxies, the central slopes are slightly steeper than for late-type galaxies (except for intermediate stellar mass galaxies, where($k_0 \approx -2.0$ dex/$R_{\rm eff}$). On the other hand, for E/S0 galaxies we estimate the central gradient only for the two most massive bins of M_*. These central gradients are similar to those derived for late-type galaxies with similar M_*. For those bins of M_* and morphology where the analysis detects an external gradient (i.e., k_1 and/or k_2), we find a mix of flatter and steeper gradients; in any case, they are still negative. Regarding the characteristic value of $\Sigma_{\rm SFR}$(i.e., measured at $R_{\rm eff}$), we find that for late-type galaxies it increases as M_* increases. For Sa-type galaxies, this $\Sigma_{\rm SFR}$ is approximately one order of magnitude smaller for a given bin of M_*. The difference is larger for E/S0 galaxies, where the characteristic $\Sigma_{\rm SFR}$ is $\approx 10^{-9.5}$ M$_\odot$ pc^{-2} yr^{-1}. These results are in good agreement with previous measurements of the gradients and characteristic values of $\Sigma_{\rm SFR}$ (Sánchez 2020).

4.3.2. *Specific SFR, sSFR*

In Figure 20 we show the results of the piece-wise analysis of the radial distribution of the sSFR (see Figure 50). We find that the values of k_0 are relatively consistent for different bins of M_* within the late-type galaxies. There is a mild increment of the slope (from negative to positive gradients) as M_* increases. As for the gradients of $\Sigma_{\rm SFR}$, the Sa galaxies lie in the only morphological bin that shows significant variations in k_0. For those bins of M_* or morphology where we measure an external gradient (k_1 or k_2) the values are usually negative. Regarding the characteristic value of the radial distribution of sSFR (i.e., at $R_{\rm eff}$), we find that it varies significantly depending on the morphology. The characteristic sSFR from early-type galaxies is at least one order of magnitude smaller in comparison to late-type galaxies. For each morphological type we do not see significant variations of the characteristic sSFR for different stellar mass bins. Qualitatively, these gradients are in agreement with previous results using a larger heterogeneous sample of galaxies (Sánchez 2020).

4.3.3. *Star-Forming Efficiency, SFE*

In Figure 21 we show the piece-wise analysis of the average of the radial distribution of the SFE segregated by morphology for different stellar mass bins (see Figure 51). Contrary to the gradients of sSFR, for the SFE the slopes for all the bins of M_* and morphology are negative (i.e., $k_0 < 0$). The value of this slope for late-type galaxies varies depending on both stellar mass and morphology ($-1.0 < k_0 < -0.4$ dex/$R_{\rm eff}$). Although for most of the radial profiles a single gradient suffices to describe the radial trend of the SFE, for some morphological bins the piece-wise analysis detected another gradient at their outskirts (k_2, e.g., Sb galaxies). We exclude from this analysis those external gradients

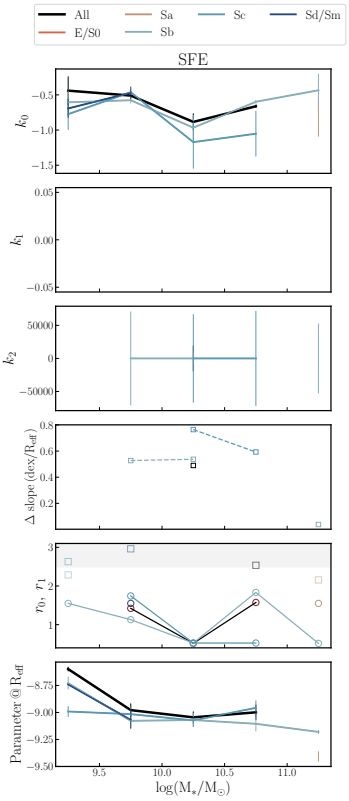

Fig. 21. Parameters derived from the piece-wise analysis for the radial distribution of the SFE. The layout of the figure is similar to Figure 4. The color figure can be viewed online.

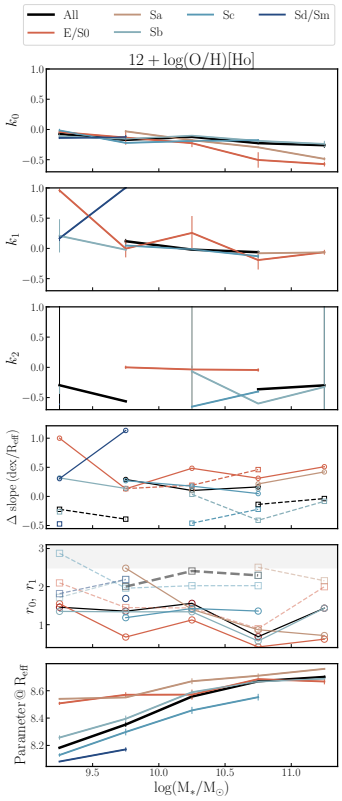

Fig. 22. The radial distribution of the oxygen abundance using the Ho calibrator. The layout of the figure is similar to Figure 4. The color figure can be viewed online.

with large values of k_2, as they are spurious. The value of this gradient depends on M_* with low and high masses having steeper gradients than the derived central values for the same mass bin. However, we note that these values may not be representative of the radial trend at these galactocentric distances, as they measure the very outer part of the galaxies. Similar to the characteristic values of sSFR, we find that for the SFE these values are similar for late-type galaxies regardless of the probed M_* (SFE $\approx 10^{-9.1}$ yr^{-1}). The trends presented here are in agreement with previous studies exploring the radial distribution of the SFE using spatially resolved observations of the molecular gas (e.g., Leroy et al. 2008; Villanueva et al. 2021).

4.4. *Chemical Abundances*

Thanks to the emission of different chemical species in the optical it has been possible to have an estimation of the amount of elements heavier than hydrogen or helium in the ISM. There is a plethora of chemical abundance calibrators in the literature, in particular of the oxygen abundance (Maiolino & Mannucci 2019, and references therein). In this analysis we present the radial distribution of the oxygen abundances using a fiducial calibrator for this abundance. However, in Appendix B we present the impact on the radial profiles of using different calibrators.

4.4.1. *Oxygen Abundance*

The oxygen abundance has been widely used to gauge the chemical stage of galaxies as well as its evolution (e.g., Maiolino & Mannucci 2019, and references therein). As we mention above, there is a large amount of abundance calibrators in the literature using different methodologies (e.g., direct estimations, photoionization models, or hybrid ones). In this section we present the analysis of the radial distribution of the oxygen abundance with an empirical calibrator derived using a neuronal network analysis from Ho (2019). Nevertheless, we present the same analysis of the radial distribution of the

oxygen abundance using different calibrators in Appendix B [10]. When necessary, we briefly discuss the differences in the results using different calibrators. Although we try to minimize the impact of other sources of ionization, we note that the radial distribution of the oxygen abundance could be affected by ionization sources other than star-formation. For this reason we consider these gradients as upper limits of the abundances.

In Figure 22 we show the result of the piece-wise analysis of the radial distribution of the oxygen abundance for the MaNGA Golden Sample (see Figure 52). We find that the central gradient, k_0, is negative regardless of the morphology or M_*. For late-type galaxies (from Sb to Sd/Sm) we find little changes of k_0 with respect to M_* with an average value of $k_0 \approx -0.13$ dex/$R_{\rm eff}$. If any, we find a slightly flatter gradient for the lowest mass bin in comparison to massive ones. Interestingly, we find similar central gradients for early-type low-mass galaxies ($\log M_* / \mathrm{M}_\odot < 10.5$). For larger masses, early-type galaxies tend to have steeper gradients in comparison to late-type ones. For those radial profiles where we are able to measure an external gradient (k_1 and k_2) we find that these gradients range from positive to negative values (with most of the k_1 slopes being positive and k_2 being negative). For the characteristic oxygen abundance (measure at $R_{\rm eff}$), we find that for late-type galaxies it increases with M_*. On the other hand, it is relatively constant for early-type galaxies 12+log(O/H) ≈ -8.6. Furthermore, massive early-type galaxies tend to have characteristic abundances similar to their late-type counterparts.

These results are in partial agreement with previous results using the MaNGA dataset and other IFS data. On the one hand, we find more subtle variations of the slope (k_0) with M_* than those reported by Belfiore et al. (2017). Differences between that study and the work presented here are expected due to the differences in the samples (selection, sizes, etc) as well as the different oxygen calibrator adopted for each work. It could also be the case that the methodology for deriving the slopes of the gradients has an impact on these different works. In this work we employ a piece-wise analysis to take into account that the radial distribution could have different gradients at different galactocentric distances, whereas Belfiore et al. (2017) employed a linear fit with a single slope to describe the radial gradient of the

[10] Oxygen and nitrogen abundances presented in this study are derived using the script `pyOxy` (`https://github.com/cespinosa/pyOxy`).

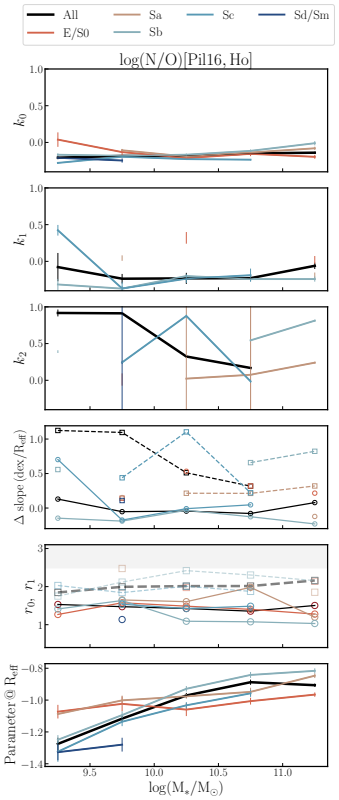

Fig. 23. The radial distribution of the N/O ratio. The layout of the figure is similar to Figure 4. The color figure can be viewed online.

oxygen abundance. On the other hand, regarding the morphology we find differences in the slope of the oxygen abundance only for early-type massive galaxies. Similar results have been reported recently using a larger sample of MaNGA galaxies (Boardman et al. 2021). Our results suggest that, at least for this sample of galaxies and for the adopted calibrator, the central gradient for late-type galaxies is rather constant for a wide range of M_*.

The above results could vary significantly depending on the adopted calibrator. In Appendix B we present a similar analysis as the one derived above using two other calibrators (the empirical calibrator O3N2 from Marino et al. 2013 and the theoretical one from Kobulnicky & Kewley 2004). In this appendix we describe the differences in the gradients depending on the used abundance calibrator. In general, we find that the adopted calibrator could have a significant impact on the derived gradients for different morphologies and stellar masses.

4.4.2. *Nitrogen/Oxygen Abundances Ratio*

Having a measurement of chemical abundances with different nucleosynthesis origins, or their ratios, allows us in principle to quantify the scales of star formation across the evolution of galaxies. On the one hand, the oxygen abundance measures the chemical enrichment from short-lived massive stars. On the other hand, the nitrogen abundance partially measures the enrichment of the ISM from stars with a smaller mass and longer lifetimes. In this section we explore the radial distribution of their ratio in our sample of MaNGA golden galaxies. For the oxygen abundance we use the same calibrator described in the previous section, whereas for the nitrogen abundance we use the calibrator derived by Pilyugin & Grebel (2016).

In Figure 23 we present the piece-wise analysis of the radial distribution of the N/O ratio for our sample of galaxies. Contrary to the oxygen abundance analysis of the previous section, we find a significant impact of both the stellar mass and morphology in setting the gradient of the N/O ratio in the central portion of our sample, k_0. For late-type Sb galaxies, k_0 increases with M_*. In other words, for this morphological type the central slope changes from negative to almost flat gradients as M_* increases. The flatness in the central region for the most massive Sb galaxies could be a consequence of the line ratios tracing diffuse ionized gas in regions dominated by a bulge, instead of tracing star formation. Thus, the measurements of the N/O ratio for the central region may not be reliable – a similar scenario is likely occurring for E/S0 low-mass galaxies. However, we note that Espinosa-Ponce et al. (2022) found similar results using a large sample of HII regions with spectroscopic information. For Sc galaxies, k_0 is negative and similar regardless of the stellar mass, except for the lowest mass bin where the slope is steeper. For Sd/Sm galaxies the slope is similar to those derived from the Sc-type. For most of the bins of morphology and M_* where the piece-wise fit is able to measure k_1, we find that it is negative, slightly steeper than k_0. However, for those bins with three gradients we find that the outer one (i.e., k_2) is positive and significantly steeper. We consider that this may be an spurious artifact due to the lax cut in SNR. This affects the radial values of the N/O ratio at the outskirts of galaxies. According to our analysis, the change in slopes for the radial distributions occurs at $\approx 1.5\ R_{\rm eff}$, regardless of the stellar mass or morphology. The characteristic values of the N/O ratio at $R_{\rm eff}$ increases monotonically with M_*, regardless of the morphology. However, for a given

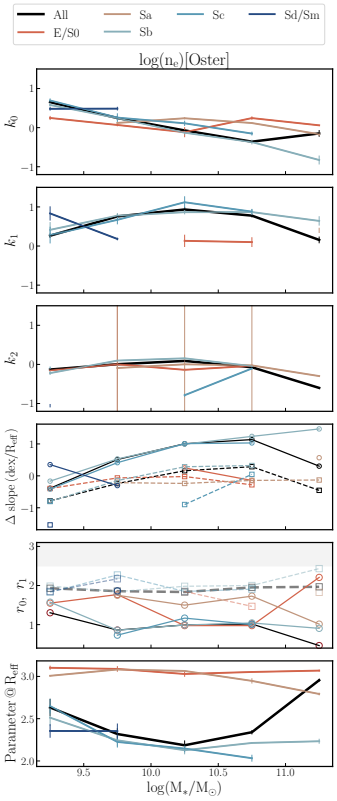

Fig. 24. The radial distribution of the electronic density derived from the Oster et al. calibrator. The layout of the figure is similar to Figure 4. The color figure can be viewed online.

stellar mass bin, the average value for the Sb galaxies is the largest in comparison to other morphological types among late-type galaxies. For early-type galaxies this characteristic value is relatively similar regardless of M_* ($\log(\mathrm{N/O}) \approx -1.0$).

Considering only our late-type sample, our central gradients from the N/O ratio differ from those derived by Belfiore et al. (2017) using a smaller sample of the MaNGA survey. Contrary to our results, they found that the gradient of the radial distribution decreases with M_*. As for the radial distribution of the oxygen abundance, these differences could be caused by the difference in the sample or by the adopted calibrators. Our results thus suggest that for late-type massive galaxies there is a flattening in the central gradient of N/O. On the other hand, using a large sample of HII regions with spectroscopic information drawn from the CALIFA survey and the same abundance calibrators, Espinosa-Ponce et al. (2022) found similar results as those derive in this study. In particular they also found flat gradients in the central part of massive Sb galaxies. This

may suggest that even when using spectral information from HII the dominant ionization mechanism detected could be due to diffuse ionized gas.

4.5. *ISM Properties*

The ratio of the flux of different emission lines allows us to provide estimations of the physical properties of the ISM. In this section we explore the radial distribution of two parameters that are fundamental to understand the energetics of the ISM, the electron density, n_e, and the ionization parameter, U.

4.5.1. *Electron Density, n_e*

Usually the electron density is estimated using the emission line ratio from a single ion. To gauge n_e, we follow Espinosa-Ponce et al. (2022). They derived this density using the [S II] doublet solving the equation:

$$\frac{[\mathrm{SII}]\lambda6717}{[\mathrm{SII}]\lambda6731} = 1.49\frac{1+3.77x}{1+12.8x}\,, \qquad (3)$$

where $x = 10^{-4} n_e t^{-1/2}$ and t is the electron temperature in units of 10^4 K (McCall et al. 1985). They assume a fiducial electron temperature expected for the usual conditions of an H II region ($t = 10^4$ K). Although this doublet is sensitive only to a narrow range of densities (≈50 to ≈7000 cm^{-3}, Osterbrock & Ferland 2006), it is still useful to gauge the radial distribution of n_e in our sample of MaNGA galaxies.

In Figure 24 we plot the results of the piecewise analysis of the radial distribution of n_e for our Golden Sample (see Figure 54). We find that the central gradient of the radial distribution of n_e, k_0, changes significantly with M_*, going from positive to negative as the stellar mass increases. We find rather flat gradients for early-type galaxies. For those galaxies where we are able to estimate an external gradient, k_1, we find steeper positive values in almost all the bins of morphology and stellar mass. We find that the characteristic electron density measure at $R_{\rm eff}$ for late-type galaxies at different stellar mass bins is relatively constant ($n_e \approx 10^{2.1} - 10^{2.5}$ cm^{-3}). On the other hand, we find larger densities for massive early-type galaxies ($n_e \approx 10^{3.0}$ cm^{-3}). Radial trends similar to those derived in this study have been reported using large spectroscopic data sets of H II regions (Espinosa-Ponce et al. 2022). These trends have been attributed to the fact that denser material is located in regions of high pressure. Usually regions of high pressure are located at the central part of galaxies with little dependence on stellar mass or morphology (Barrera-Ballesteros et al. 2021).

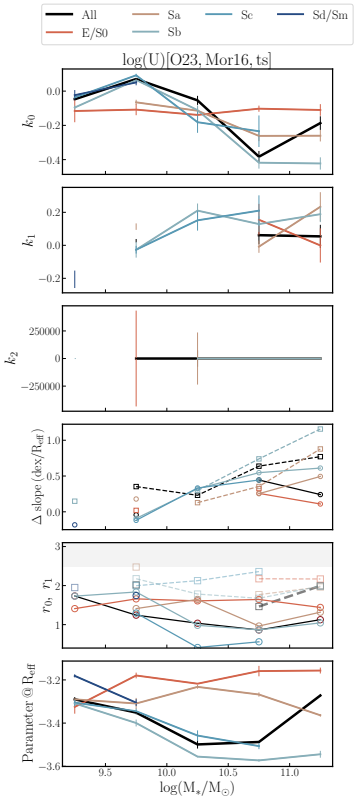

Fig. 25. The radial distribution of the ionization parameter derived from the calibrator presented by Morisset et al. (2016). The layout of the figure is similar to Figure 4. The color figure can be viewed online.

4.5.2. *Ionization Parameter*

The ionization parameter (U) measures the ratio between the number of ionizing photons and the number of atoms of hydrogen. Despite its importance, it is rather difficult to estimate U observationally. Although it is usually gauged using emission line ratios from a given element (e.g., [O III]/[O II]), this parameter depends on the geometry of the explored regions, and the hardness of the ionizing spectra, among other properties. For this study, we estimate the ionization parameter and the above line ratio. We follow the relation derived from recent photoionization models from Morisset et al. (2016).

In Figure 25 we show the results from the piecewise analysis of the radial distribution of the ionization parameter in our sample (Figure 55). In contrast to the early-type galaxies where the central gradient has small variations ($k_0 \approx -0.1$ dex/$R_{\rm eff}$), late-type galaxies have significant variations of their central gradients for different bins of stellar mass. Late-type galaxies in the lowest mass bin tend to have a similar negative gradient as those derived

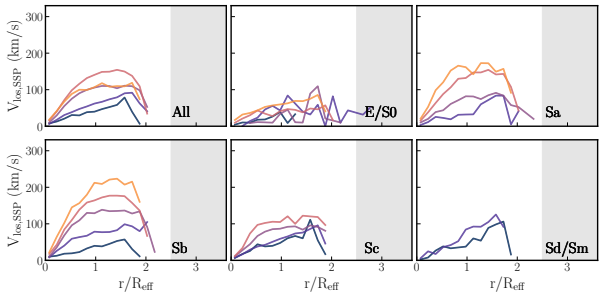

Fig. 26. The average radial distribution of the line-of-sight stellar velocity, $V_{\rm los,SSP}$. Similar to the distribution of Figure 3, the gradients are averaged by stellar mass and morphology. In each panel, each solid line represents the average profile per total stellar mass bin. The color figure can be viewed online.

for early-type galaxies, whereas for the next mass bin ($\log(M_*/{\rm M}_\odot) < 9.7$) we find that galaxies have a positive gradient. For the next two mass bins, late-type galaxies have negative gradients with k_0 decreasing as M_* increases. For the most massive bin (where it is only possible to measure the central gradient from Sb galaxies) k_0 remains with a similar negative slope as in the previous mass bin. Regardless of the stellar mass or the morphology, we find positive steep gradients in the outskirts of the galaxies in our sample. We find that the characteristic value of U measured at $R_{\rm eff}$ decreases with M_* for late-type galaxies, whereas for early-type objects this value of U is relatively constant for different bins of M_* ($U \approx 10^{-3.2}$). Qualitatively, our results are in partial agreement to those derived using a sample of H II regions from the CALIFA survey (Espinosa-Ponce et al. 2022), namely that in the central region of the galaxies the slopes of the gradients of U are usually negative or mildy possitive.

5. KINEMATIC PROPERTIES

To provide a reliable estimation of the properties of the stellar component from the continuum, the SSP fitting technique must be able to also provide an estimation of at least the first two moments of the line-of-sight velocity distribution (LOSVD) of the stellar component. In a similar fashion, the emission-line analysis should also provide an estimation of at least the two moments of the LOSVD of the ionized gas. Given the fact that the kinematic radial profiles follow different trends and that their shape is usually fitted by a non-linear function (e.g., López-Cobá et al. 2017; Barrera-Ballesteros et al. 2018), in this section we will provide a qualitative description of these kinematic features.

In Figure 26 we plot the radial distribution of the first moment of the LOSVD, $V_{\rm los,ssp}$, averaged for different stellar masses and morphologies. To create these radial profiles of $V_{\rm los,ssp}$ for each galaxy and each radial bin, we averaged the absolute values of velocity from the receding and the approaching sides of the stellar velocity field. The shape of the $V_{\rm los,ssp}$ profiles segregated only by stellar mass depends strongly on it (top left panel of Figure 26): massive galaxies exhibit a rising profile with a flattening at ≈ 1.5 $R_{\rm eff}$, whereas low-mass galaxies shows a monotonically increasing of $V_{\rm los,ssp}$. Furthermore, the absolute values of each radial profile increase with the stellar mass (e.g., measuring $V_{\rm los,ssp}$ at $R_{\rm eff}$), except for the most massive bin where the radial profile $V_{\rm los,ssp}$ is below the profile from the second most massive bin. We also find that, regardless of M_*, at large galactocentric distance $V_{\rm los,ssp}$ has a significant drop. These drops could be indicating the maximum radii at which it is possible to have a reliable measurement of the rotational curve for the galaxies; beyond those radii the measurements of the SNR of the continuum may not allow a proper estimation of $V_{\rm los,ssp}$. For consistency with the radial analysis of the other stellar properties we do not attempt any further selection of the radial profiles of $V_{\rm los,ssp}$. Segregated by morphology and stellar mass, the radial profiles of $V_{\rm los,ssp}$ reveal interesting features. For E/S0 galaxies (top middle panel of Figure 26) we find strong radial variations of $V_{\rm los,ssp}$ for different bins of M_*, except for the most massive bin, where we observe a monotonic increment of $V_{\rm los,ssp}$ with radius. These strong variations could suggest that early-type galaxies are supported by random motions instead of ordered ones. However, when we plot the radial distribution of the $\lambda_{\rm ssp}$ parameter, we find that these galaxies appear to be supported by these two components. We will come to this point below. For Sa galaxies we find a trend for the radial distributions of $V_{\rm los,ssp}$ similar to those observed using the entire GS for different bins of M_*; the gradient of $V_{\rm los,ssp}$ becomes steeper as M_* increases. Only the lowest probed mass bin shows a monotonically increment of $V_{\rm los,ssp}$, while the other profiles show a plateau at large galactocentric distances. For late-type galaxies (Sb, bottom left panel of Figure 26) we find that the shape of the radial profile of $V_{\rm los,ssp}$ varies for different stellar masses. Massive galaxies show a steeper gradient, and a flattening at large radii in comparison to low-mass galaxies that exhibit a monotonically increase of $V_{\rm los,ssp}$. For Sc galaxies (bottom middle panel of Figure 26) we observe a monotonically increment of $V_{\rm los,ssp}$ with radius, with

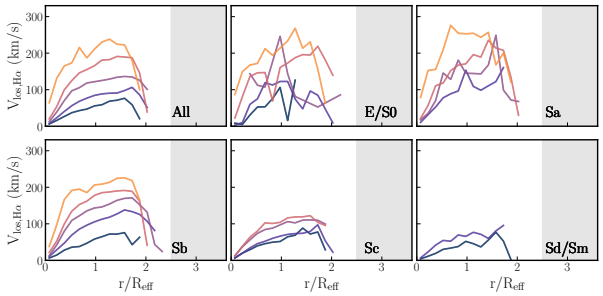

Fig. 27. The radial distribution of the line-of sight ionized gas velocity, $V_{\rm los,H\alpha}$. The layout of the figure is similar to Figure 26. The color figure can be viewed online.

little dependence on the stellar mass. As for the other stellar properties, for Sd/Sm galaxies we are able to measure the radial gradients of $V_{\rm los,ssp}$ only for low-mass galaxies. Thus the radial profiles of $V_{\rm los,ssp}$ show a monotonical increase with no signature of a plateau.

In comparison to $V_{\rm los,ssp}$, we find similar trends in the radial distribution of the velocity derived for the ionized gas, $V_{\rm los,H\alpha}$ (Figure 27). Averaging the gradients only over stellar mass, the increments for massive galaxies are stepper in comparison to low-mass galaxies. Similar trends are also observed when we average $V_{\rm los,H\alpha}$ over morphology and M_* bins in comparison to those derived for $V_{\rm los,ssp}$. Although the radial averages are similar, we note that $V_{\rm los,H\alpha}$ shows larger velocities in comparison to $V_{\rm los,ssp}$.

To further quantify these differences, we plot in Figure 28 the radial distribution of the $V_{\rm los,H\alpha}/V_{\rm los,ssp}$ ratio using the radial profiles of $V_{\rm los,H\alpha}$ and $V_{\rm los,ssp}$ presented in Figures 27 and 26, respectively. We find interesting features for the radial profiles of this ratio. When segregating the entire GS only by M_* we find that the most massive M_* bin shows a significant increment of $V_{\rm los,H\alpha}$ in comparison to $V_{\rm los,ssp}$ across the optical extension of the galaxies; furthermore, the radial profile of the $V_{\rm los,H\alpha}/V_{\rm los,ssp}$ ratio spikes at the central region of the galaxies with $V_{\rm los,H\alpha}/V_{\rm los,ssp} \approx 4$. For the rest of the stellar mass bins, the shape and values of this ratio are relatively similar. For the very center of galaxies the ratio is slightly below, or close to, 1. As the galactocentric distance increases this ratio remains relatively constant with $V_{\rm los,H\alpha}/V_{\rm los,ssp} \approx 1.2$; for radii larger than $r/R_{\rm eff} \approx 1.5$, this ratio drops to values close to zero. For early-type galaxies, this ratio strongly varies across the radial extension of the galaxies; therefore, it is not possible to provide a reliable description of it. For massive Sa galaxies ($\log(M_*/{\rm M}_\odot) \gtrsim 10.5$) we find that the radial profiles of the $V_{\rm los,H\alpha}/V_{\rm los,ssp}$ ratio have similar shapes and values as those derived for the entire sample. Sa galaxies with smaller stellar mass exhibit strong variations in the radial profiles of their velocity ratio. Except for the lowest-mass bin of Sb galaxies, these galaxies show a rather constant $V_{\rm los,H\alpha}/V_{\rm los,ssp}$ ratio across their optical extension, $V_{\rm los,H\alpha}/V_{\rm los,ssp} \approx 1.4$. Low-mass galaxies exhibit a rising profile reaching a peak of $V_{\rm los,H\alpha}/V_{\rm los,ssp} \approx 2$ at $r/R_{\rm eff} \approx 1.2$. After this radius the ratio decreases to values close to zero. For Sc galaxies the radial distribution of this ratio is relatively constant for the different mass bins ($V_{\rm los,H\alpha}/V_{\rm los,ssp} \approx 1$). Finally, for the Sd/Sm galaxies the $V_{\rm los,H\alpha}/V_{\rm los,ssp}$ ratio decreases as the radius increases. We note that we are only able to estimate this ratio for low-mass galaxies. Although the ratio at the center of these galaxies is larger than 1, it decreases reaching values close to zero at their outskirts. This analysis highlights the well-known interplay between the morphology and kinematic structure of galaxies (e.g., Cappellari 2016). For Sa galaxies, where the $V_{\rm los,H\alpha}/V_{\rm los,ssp}$ ratio is the largest, $V_{\rm los,H\alpha}$ traces ionized gas probably located in the mid-plane of the galaxy, whereas $V_{\rm los,ssp}$ is coupled with non-ordered motion in the line-of sight. On the other hand, for late-type galaxies both stars and ionized gas trace similar velocities, as both trace the ordered motions from the disk.

The SSP as well as the emission line analysis provides an estimation of the second momentum of the LOSVD, also known as the stellar and ionized gas velocity dispersions, ($\sigma_{\rm ssp}$, $\sigma_{\rm H\alpha}$, respectively). In Figure 29 we plot the radial distribution of $\sigma_{\rm ssp}$ for different stellar masses and morphologies. The top left panel of this figure shows the large impact that stellar mass has in the radial profiles of $\sigma_{\rm ssp}$. Massive galaxies ($\log M_*/{\rm M}_\odot > 11.0$, dark red profile) have the largest values of $\sigma_{\rm ssp}$. The central velocity dispersion for these massive galaxies reach the largest value (≈ 200 km s^{-1}) and their average radial profile decreases with galactocentric distance. For the lowest stellar mass bin ($10.5 < \log M_*/{\rm M}_\odot < 11.0$, yellow profile), the shape of the $\sigma_{\rm ssp}$ radial profile is similar, although its central value is significantly smaller than the one derived for the most massive galaxies; for large radius it reaches a flat gradient close to 10 km s^{-1}. For the remaining stellar mass bins the radial profiles are basically flat with a constant velocity dispersion of ≈ 10 km s^{-1}. For massive E/S0 galaxies $\sigma_{\rm ssp}$ decreases with radius; the central dispersion for the most massive galaxies is the largest of the entire sample (≈ 250 km s^{-1}). For

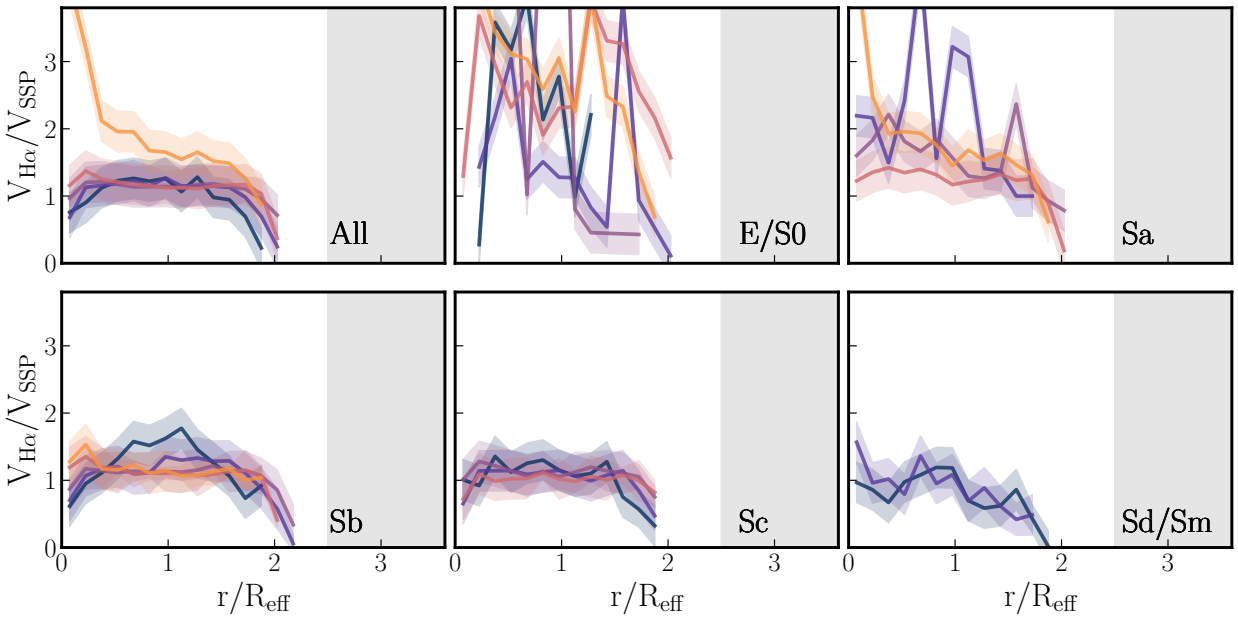

Fig. 28. The ratio of the radial profiles presented in Figures 27 and 26. The shaded area represents the standard deviation of the radial distribution in each radial beam. The layout of the figure is similar to Figure 26. The color figure can be viewed online.

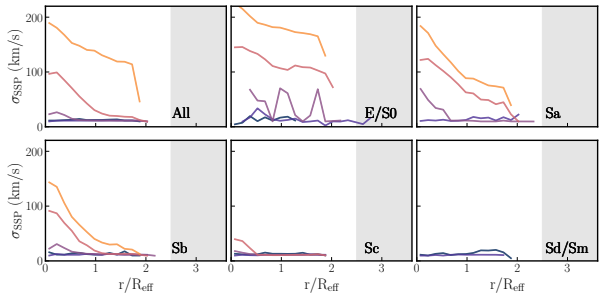

Fig. 29. The radial distribution of the stellar velocity dispersion, $\sigma_{\rm SSP}$. The layout of the figure is similar to Figure 26. The color figure can be viewed online.

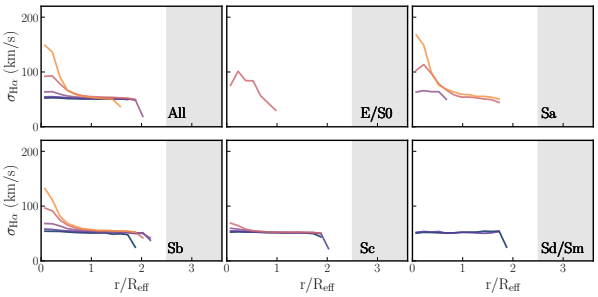

Fig. 30. The radial distribution of the stellar velocity dispersion, $\sigma_{\rm H\alpha}$. The layout of the figure is similar to Figure 26. The color figure can be viewed online.

low-mass E/S0 the radial profiles are flat, with values close to 0 km s^{-1}. Sa galaxies show a similar trend as those described for E/S0 galaxies, although the drop of $\sigma_{\rm ssp}$ with radius is sharper for massive Sa galaxies than for their E/S0 counterparts. For Sb galaxies the trends are similar to Sa galaxies. However, the drop for massive galaxies is even sharper than for Sa galaxies. For Sc and Sd/Sm galaxies we report flat gradients of $\sigma_{\rm ssp}$ with dispersions close to 0 km s^{-1}.

Similar to $\sigma_{\rm ssp}$, in Figure 30 we plot the radial distribution of $\sigma_{\rm H\alpha}$. We find similar trends for different stellar masses and morphologies in comparison to those reported above for $\sigma_{\rm ssp}$. However, we note two significant differences. On the one hand, the flattening of the $\sigma_{\rm H\alpha}$ radial profiles occurs at a higher velocity dispersion than for $\sigma_{\rm ssp}$. This is expected, since the estimation of $\sigma_{\rm H\alpha}$ is significantly limited by the spectral resolution of the instrument ($\approx$ 45 km s^{-1}, Law et al. 2021). On the other hand, we find smaller values of $\sigma_{\rm H\alpha}$ in comparison of $\sigma_{\rm ssp}$, as well as sharper drops of the velocity dispersion for massive galaxies. To account for these differences we follow a similar analysis as for the line-of-sight velocities, namely, we derive the ratio $\sigma^{corr}_{\rm H\alpha}/\sigma_{\rm ssp}$, where $\sigma^{corr}_{\rm H\alpha}$ considers a correction in quadrature to $\sigma_{\rm H\alpha}$ in order to account for the instrumental resolution ($\sigma^{corr\,2}_{\rm H\alpha} = {\sigma_{\rm H\alpha}}^2 - \sigma^2_{ins}$), with σ_{ins} = 45 km s^{-1} (Sanchez et al., submitted).

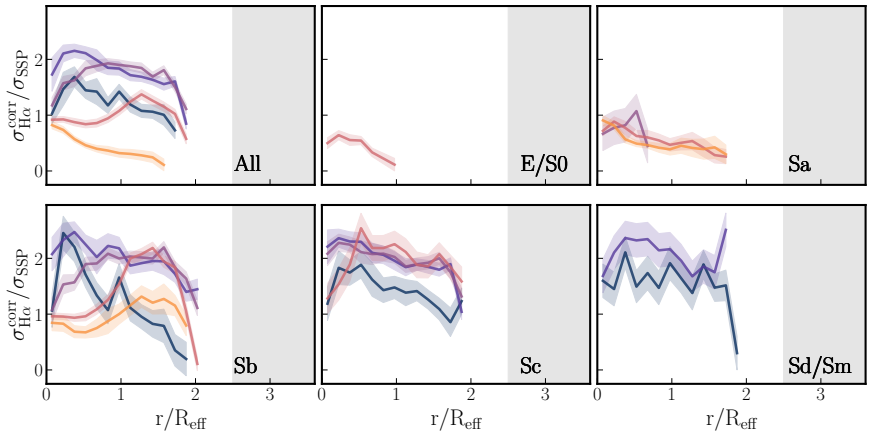

Fig. 31. The radial distribution of the $\sigma^{corr}_{\rm H\alpha}/\sigma_{\rm ssp}$ ratio. The layout of the figure is similar to Figure 26. The color figure can be viewed online.

In Figure 31 we show the radial distribution of the above ratio. When the sample is segregated only by stellar mass (top left panel), we observe different trends for the different stellar mass bins. For low and intermediate-mass galaxies we find that for the radial profiles $\sigma^{corr}_{\rm H\alpha}/\sigma_{\rm ssp}> 1$, suggesting that $\sigma_{\rm H\alpha}$ across these galaxies is larger than $\sigma_{\rm ssp}$. Furthermore the radial profiles of this ratio increase and peak up to certain galactocentric distance ($r/R_{\rm eff} \approx 0.5$); beyond this radius this ratio decreases with distance. On the other hand, for the most massive galaxies $\sigma^{corr}_{\rm H\alpha}/\sigma_{\rm ssp} < 1$ for all the radial bins. Although the central value is close to one, this ratio decreases with radius reaching values close to zero. For the intermediate stellar mass bin ($10.5 < \log M_*/{\rm M}_\odot < 11.0$, yellow profile) the central portion of the ratio is rather flat with $\sigma^{corr}_{\rm H\alpha}/\sigma_{\rm ssp}\approx 1$. However, at $r \approx R_{\rm eff}$ this ratio increases to ≈ 1.5, suggesting that for galaxies of that M_*, the dispersions are similar in their central portion, with an increase of $\sigma_{\rm H\alpha}$ at larger radii in comparison to $\sigma_{\rm ssp}$.

For early-type galaxies (top middle panel of Figure 31), we are able to make this comparison only for one stellar mass bin ($10.5 < \log M_*/{\rm M}_\odot < 11.0$, yellow profile). This profile shows $\sigma^{corr}_{\rm H\alpha}/\sigma_{\rm ssp} < 1$ with values decreasing with radius. As expected, $\sigma_{\rm ssp}$ is larger for E/S0 galaxies in comparison to $\sigma^{corr}_{\rm H\alpha}$. For Sa galaxies the radial distributions of $\sigma^{corr}_{\rm H\alpha}/\sigma_{\rm ssp}$ decreases with radius. However, all the values are below 1, except for the lowest mass bin sampled, although the values are highly variable. For these galaxies, as for the E/S0 sample, $\sigma_{\rm ssp}$ dominates over $\sigma^{corr}_{\rm H\alpha}$. For late-type Sb galaxies we find different trends for different mass bins (bottom left panel of Figure 31). The most massive Sb galaxies show central values of $\sigma^{corr}_{\rm H\alpha}/\sigma_{\rm ssp}$ slightly smaller than 1. However, as the galactocentric distance increases $\sigma^{corr}_{\rm H\alpha}/\sigma_{\rm ssp}$ has values above one for radii beyond 1.5 $R_{\rm eff}$. This change in tendency suggests that although for the central portion of massive Sb galaxies $\sigma_{\rm ssp}$ is larger than $\sigma^{corr}_{\rm H\alpha}$, at larger radii the situation is the other way around: turbulent motions of the ionized gas component dominate the ones from the stellar component. The lower mass bin of Sb galaxies (yellow profile) has a similar, yet more evident, radial trend of the $\sigma^{corr}_{\rm H\alpha}/\sigma_{\rm ssp}$ ratio in comparison to the red profile. For distances smaller than the $R_{\rm eff}$ this ratio is 1. However, it increases reaching values close to 2 around 1.5 $R_{\rm eff}$. Regardless of the galactocentric distance, we find for intermediate mass bins that the $\sigma^{corr}_{\rm H\alpha}/\sigma_{\rm ssp}$ ratio is larger than 1. For Sb galaxies with $10.0 < \log M_*/{\rm M}_\odot < 10.5$ (cyan profile), we find that this ratio increases with radius up to $R_{\rm eff}$; beyond that point the ratio is relatively flat reaching a constant value of $\sigma^{corr}_{\rm H\alpha}/\sigma_{\rm ssp}$ ≈ 2. For Sb galaxies with $9.5 < \log M_*/{\rm M}_\odot < 10.0$, the dispersion ratio decreases with distance from $\approx$2 to 1. For Sb galaxies, the radial profile with the sharpest variation of this ratio is the one corresponding to the lowest mass bin ($9.5 < \log M_*/{\rm M}_\odot$, dark-blue profile). For Sb galaxies, these objects have the largest $\sigma^{corr}_{\rm H\alpha}/\sigma_{\rm ssp}$ ratio at their center. However, as the galactocentric distance increases this ratio decreases, reaching values close to zero at their outskirts. For Sc galaxies, the $\sigma^{corr}_{\rm H\alpha}/\sigma_{\rm ssp}$ ratio is larger than 1 regardless of the probed stellar mass and radii. In general, for the probed bins of M_* we find that this ratio decreases with distance, with values close to 2 in the center to values close to 1 in

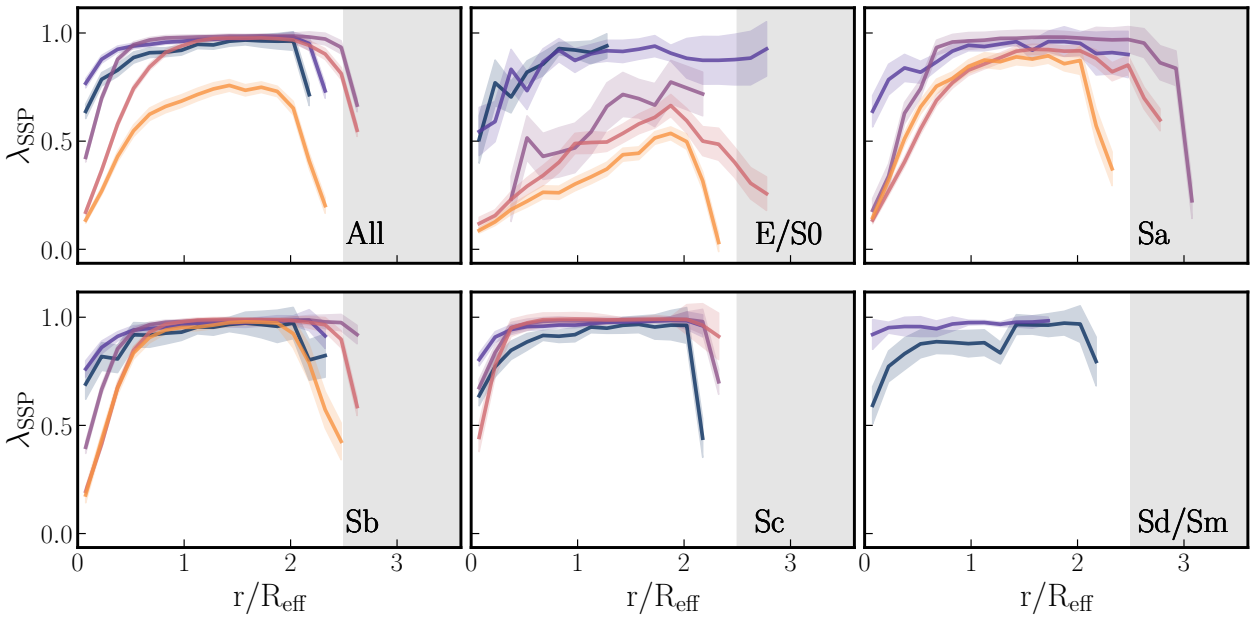

Fig. 32. The radial distribution of the λ parameter for the stellar component. The layout of the figure is similar to Figure 5. The color figure can be viewed online.

their outskirts. Finally, for the Sd/Sm galaxies we also find that this ratio is larger than 1 for the probed bins of M_* (low-mass galaxies) and radii. The values of this ratio are relatively constant for different radii, with $\sigma^{corr}_{\rm H\alpha}/\sigma_{\rm ssp} \approx 1.5$ - 2.

Thanks to the spatially resolved information of the MaNGA survey, we are able to probe the kinematic stage of the demographics in the nearby universe by comparing the kinematic properties of the stellar and the ionized gas. Furthermore, these radial profiles are also useful to explore dynamical differences in these components. For instance, by measuring the differences between $V_{\rm los,ssp}$ and $V_{\rm los,H\alpha}$ as well as $\sigma_{\rm ssp}$ and $\sigma^{corr}_{\rm H\alpha}$ we are able to explore how each of these components traces the potential well of the galaxies.

In Figure 32 we plot the radial distribution of the so-called apparent spin parameter for the stellar component $\lambda_{\rm ssp}$ (Emsellem et al. 2007) for different stellar masses and morphologies. This parameter is defined as:

$$\lambda_{\rm ssp} = \frac{\sum_{r'<r} f_\star \; r \; |v_\star|}{\sum_{r'<} f_\star \; r' \; \sqrt{v_\star^2 + \sigma_\star^2}}, \qquad (4)$$

where $f_\star$, $v_\star$ and $\sigma_\star$ correspond to the stellar flux-intensity in the V-band at any position (x, y) within the FoV, the stellar velocity and the stellar velocity dispersion in each spaxel within the considered apertures, and r is the deprojected galactocentric distance. $\lambda_{\rm ssp}$, which varies between 0 and 1, and gauges what sets the kinematic structure of a galaxy (Cappellari 2016). Values of $\lambda_{\rm ssp}$ close to 1 suggest that the region/galaxy is rotationally supported, whereas values close to zero suggest that the region/galaxy is supported by non-ordered motions. In general $\lambda_{\rm ssp}$ increases with distance, although the central shape of this increment varies depending on the stellar mass and morphology. Segregated only by stellar mass, the central value of $\lambda_{\rm ssp}$ decreases with M_*. This parameter increases steeply with distance, reaching the value of 1 at small galactocentric distances for most of the stellar mass bins, except for the most massive bin, where the radial profiles of $\lambda_{\rm ssp}$ reach a plateau at $\lambda_{\rm ssp} \approx 0.7$. For E/S0 galaxies the radial distributions of $\lambda_{\rm ssp}$ vary significantly depending on M_*. For low-mass galaxies the radial distribution rises very steeply becoming almost flat with values close to 1. For intermediate-mass and massive galaxies the radial profiles of $\lambda_{\rm ssp}$ monotonically increases. We note that the two more massive bins show a strong drop of $\lambda_{\rm ssp}$ at their outskirts. As we mention above, kinematic properties such as $V_{\rm los,ssp}$ may not be reliable at large radii due to our conservative cuts in SNR. These results suggest that for galaxies with this morphology the stellar mass plays a major role in setting the kinematic stage of the stellar component; low-mass E/S0 galaxies appear to be kinematically supported by rotation, while massive

E/S0 galaxies are supported by random motions or rotation, depending on the location. For the rest of the morphological bins the trends are similar for different bins of M_*. Most of the profiles exhibit an almost flat radial distribution close to 1 – except for the most massive galaxies. Other than the E/S0 morphological bin, we are able to measure the radial profile of $\lambda_{\rm ssp}$ for the most massive stellar bin only for Sa and Sb galaxies. In these morphological bins the radial profile of the most massive bin shows a sharp drop in their central region, suggesting that for these galaxies their centers are supported by random motions while the rest of the galaxy is supported by ordered motions. These results highlight the fact that, in comparison to morphology, M_* appears to play a major role in setting the radial distribution of $\lambda_{\rm ssp}$.

6. RADIAL PROFILES FROM THE ENTIRE MANGA SAMPLE

As we mention in § 2.2, in order to provide a reliable estimation of the radial distribution of the physical properties, we select from the entire MaNGA sample ($\approx$ 10000 targets) those galaxies that satisfy several criteria, including good radial coverage from the fiber bundle as well as reliable spatial sampling and resolution. These selection criteria yield what we refer in this study as the *Golden Sample, GS* ($\approx$ 13 % of the entire MaNGA sample). In this section we derive the radial distribution of the physical properties studied above for a much larger sample of MaNGA galaxies. The only selection criteria for this analysis is low-inclined galaxies (i.e., the major/minor axis ratio has to be smaller than 0.45). This criterion yields a sample of $\approx$ 7500 galaxies. Evidently, the entire sample provides a much better coverage on M_* and morphology. Since the GS includes those galaxies with the best spatial coverage and resolution, here we only provide a qualitatively comparison between the radial profiles from the GS and those derived from the entire sample. We refer the reader to the following web page, where we include the same analysis for the entire sample: `http://ifs.astroscu.unam.mx/MaNGA/Pipe3D_v3_1_1/radial/figures/`

M/L ratio, and Σ_*: In general, the radial profiles of the M/L ratio for the entire sample show negative trends similar to those derived for the GS (see Figures 4 and 33). As for the GS, the central gradient of the radial profiles of M/L ratio depends mainly on M_*. Furthermore, the characteristic value of this ratio strongly depends on the morphology. Similarly, for the entire sample the radial profiles of Σ_* decrease with radius as for the GS. However, we note sharp drops at large radii for low-mass galaxies regardless of the morphology. On the other hand, contrary to the GS, the characteristic value of Σ_* for the entire sample appears to depend strongly on both M_* and morphology.

Stellar age, metallicity, and extinction: The central gradients of the stellar age are slightly flatter for the entire sample in comparison to the GS. As for Σ_*, we note that for some bins of morphology and M_* the age shows a sharp drop at the outskirts of galaxies. As for the gradients of stellar metallicity, although we find similar negative central slopes in both the complete and the Golden Sample, for the entire sample we find step positive external gradients in different bins of morphologies and stellar mass. As for other measurements, such as those derived from the emission lines, we are finding that for galaxies with positive gradients at the outskirts the continuum flux is dominated by the noise; therefore those values of metallicity are not reliable. Finally, for the optical extinction we find that the gradients of the entire sample are similar to the GS; however, they are slightly smoother, that is, the gradients at the outskirts tend to be similar to those derived for the central part of galaxies.

Emission lines fluxes, EW(Hα), and line ratios: Although the general behavior of the slopes of the radial gradients of different emission lines (Hα,Hβ, [NII], and [OIII]) for the entire sample is similar to the one measured from the GS (i.e., negative gradients), we find that regardless of the emission line, the central gradients for early-type galaxies are similar to those derived for late-type galaxies. We recall that in § 4.1 we found that the early-type galaxies showed sharper negative gradients in comparison to late-type for the probed bins of M_*. In contrast to the GS, in the eintire sample it is more difficult to observe the difference between the characteristic flux measured at $R_{\rm eff}$ for early-type galaxies and for late-type ones. For the radial distribution of the EW(Hα) using the entire sample, we find similar trends as those measured in the GS, both in slopes and characteristic radii. As we discuss in the next section, we consider that those variations in the gradients are caused mainly by the impact of the bulge. Regarding the radial distribution of the emission line ratios (Hα/Hβ, [NII]/Hα, and [OIII]/Hβ), we find trends similar to the GS, as well as similar characteristic values. Other properties derived from the emission line ratios for the entire sample, such as $\rm Av_{gas}$, the $\rm Av_{gas}/Av_{SSP}$ ratio, $\Sigma_{\rm mol,Av}$, and $\rm f_{mol}$, show ra-

dial distributions similar to those derived from the GS.

$\Sigma_{\rm SFR}$, sSFR, and SFE: The radial distribution of the $\Sigma_{\rm SFR}$ for the entire sample is similar to the one derived for the GS. We find a negative gradient across the entire extension of the galaxies. Although we note some deviations from this gradient depending on the stellar mass and morphology (e.g., an almost flat gradient for the lowest-mass bin of early-type galaxies). The characteristic values of $\Sigma_{\rm SFR}$ measured at $R_{\rm eff}$ vary depending on both M_* and the morphology: they usually increase from early to late type galaxies for a given bin of M_*. Similar to the GS, the entire sample shows an almost flat gradient for the sSFR (although at large radii some profiles show drops), regardless of the stellar mass and morphology. As for the GS, there is a clear segregation between the sSFR measure at $R_{\rm eff}$ for early and late-type galaxies: early galaxies have significantly smaller sSFR in comparison to late-types for the same stellar mass bin. For the radial distribution of the SFE we find a characteristic negative gradient regardless of the stellar mass and morphology. However, we find significant variations of the SFE measured at $R_{\rm eff}$ for both stellar bins of M_* and morphology.

Oxygen abundance, N/O ratio, electron density, and ionization parameter: The radial distribution of the oxygen abundance using the entire sample, and the Ho calibrator (Ho 2019), is very similar to the one derived from the GS adopting the same calibrator. However, the piece-wise analysis provides a better description of the radial profiles when using the entire sample in comparison to the GS. For the entire sample, the slope of the central gradient decreases, k_0 with M_*. It is important to note, that the extension of the central gradient also varies depending on M_*. The extension where the piece-wise analysis detects k_0 is significantly smaller for massive galaxies in comparison to galaxies with lower mass. When comparing the large extension of the galaxies, the slope of the radial distribution is similar for different bins of M_* ,except for the lowest-mass bin, where the slope is flatter in comparison to other mass bins. The characteristic oxygen abundances are the same, regardless of the sample. These results are in agreement with those presented previously in the literature using the same sample of galaxies (e.g., Barrera-Ballesteros et al. 2016; Boardman et al. 2021). We also find similar distributions for the N/O ratio, the electron density, and the ionization parameter for both samples. These results suggest that the GS is a representative sample of the entire MaNGA sample regarding the estimation of radial properties of the ionized gas.

Stellar and ionized gas kinematics: For the entire sample we find that the radial distribution of $V_{\rm los,ssp}$ is similar to the one derived for the GS for most of the bins of morphology and M_*. We only find significant differences for E/S0 low-mass galaxies: instead of strong radial variations in $V_{\rm los,ssp}$, we find that their radial profile is flat and close to zero km s $^{-1}$. Similar to $V_{\rm los,ssp}$, we find common trends between the entire sample and the GS for the radial distribution of $V_{\rm los,H\alpha}$. As above, the entire sample provides a smoother radial profiles of $V_{\rm los,H\alpha}$ for E/S0 galaxies in comparison to those derived for the GS. From the comparisons above it is clear that the radial distribution of the $V_{\rm los,H\alpha}/V_{\rm los,ssp}$ ratio is similar when using the entire sample or the GS. Nevertheless, we note that for the entire sample the most massive E/S0 galaxies are those responsible for the large ratio observed for the entire population of massive galaxies (e.g., top left panel of Figure 28). Although the radial distribution of both $\sigma_{\rm ssp}$, and $\sigma_{\rm H\alpha}$ are similar for both the entire and the GS, we find significant differences when we compare the radial distribution of the $\sigma^{corr}_{\rm H\alpha}/\sigma_{\rm ssp}$ ratio between the two samples. Contrary to the GS, the radial distribution of this ratio when using the entire sample segregated only by M_* is relatively flat and close to one. Similar trends are observed for the Sb galaxies. Finally, we find similar radial trends for $\lambda_{\rm ssp}$ between the entire sample and the GS. The above results show that the most significant difference, kinematically speaking, when using a sample that provides the best conditions to derive radial profiles and the entire MaNGA sample is observed in their velocity dispersion of both components. This could indicate that, rather than affecting the systemic velocity of the galaxies, using a large sample of galaxies averages a non-linear property such as the velocity dispersion.

7. DISCUSSION

Along this study we explore the radial distribution of the different physical properties that can be derived from the optical spectra (i.e., the stellar and ionized gas properties). We use a piece-wise analysis to account for possible variations on the slopes of the gradients from those radial distributions. In general, we find that for those parameters that relate to an absolute property, a gradient with a single slope usually suffices to describe them (e.g., Σ_*, $\rm Av_{SSP}$, emission-line fluxes). On the other hand, we find that for some relative properties a gradient with different slopes is needed to provide a good rep-

resentation of the radial distribution of those parameters (e.g., M/L, EW(Hα), emission-line ratios). We also find that the election of a gradient with a single or several slopes for the radial distribution of a given property also depends on both the morphology and the stellar mass: for a significant fraction of parameters the slopes for early-type galaxies differ from those measured for late-type ones. This is also valid for the absolute values of the radial distributions (measured by their characteristic value at $R_{\rm eff}$).

One of the physical properties that best exemplifies the need of using gradients with different slopes to describe its radial distribution is the EW(Hα): see the piece-wise analysis and the radial distribution in Figures 10 and 41, respectively (see also the line ratios [NII]/Hα and [OIII]/Hβ). As we describe in § 4.1, the signs of the slopes vary from positive to negative for the central and external parts of the radial distribution of the EW(Hα), respectively. This transition of gradients is evident for Sb galaxies, regardless of the total stellar mass. On the other hand, early-type galaxies (E/S0, Sa) show a flat gradient regardless of M_* . As we mention in § 4.1 the EW(Hα) measures the star-formation activity. Thus, regions with an EW(Hα) $\lesssim$ 6Å correspond to an ionization source different than star formation (e.g., diffuse ionized gas, DIGs, from HOLMES), whereas larger values of EW(Hα) are associated with star-formation: the larger the value of EW(Hα) the more star-formation activity is occurring.

The change in the slopes for Sb galaxies reflects what we consider is the impact of the galaxy's structure, in particular, the presence of a bulge in the center of galaxies. For instance, the central value of EW(Hα) from the most massive Sa galaxies is similar to those derived from E/S0 and Sa galaxies (i.e., below 6Å) suggesting that even though the galaxy has a late-type morphology in its center it has properties similar to an early-type galaxy. As the galactocentric distance increases the EW(Hα) increases reaching a peak around $\approx 1.2R_{\rm eff}$. This could indicate a composite stage where DIGs and star-forming regions cohabit, and as the galactocentric distance increases the star-formation increases overcoming the contribution from DIGs, reaching a maximum contribution at $\approx 1.2R_{\rm eff}$. For galactocentric distances larger than $\approx 1.2R_{\rm eff}$, EW(Hα) decreases with radius reaching again values below 6Å. The slope of this decrease is similar to the negative slope derived from other late-type galaxies (Sc and Sd/Sm). This indicates that for farther distances the properties of an Sb galaxy resemble those expected for late-type galaxies. Our results thus suggest that particular types of galaxies, such as the Sb galaxies, can be considered as a composition between an early-type galaxy in their center and a disk one in their outskirts.

Using IFS data, different works have suggested a similar scenario for galaxies with bulges. Using a photo-spectral decomposition of galaxies Méndez-Abreu et al. (2019) obtain the spectra for individual structural components of S0 galaxies, in particular, their bulges and disks (see also, Johnston et al. 2017; Méndez-Abreu et al. 2021). They find that indeed the physical properties of these galaxies are different between their center and their outskirts. For instance, the properties of the ionized gas in the central region resemble those of early-type galaxies, whereas the properties of the outskirts are consistent with those derived from late-type galaxies. In other words, our results suggest that for those galaxies where we find significant differences in the slopes of their gradients, this is due to the fact that the physical properties are different across their optical extension. Furthermore, for bulge galaxies our results also agree with the scenario in which bulges (or central parts of the galaxies) were formed at early ages of the universe, either by monolithic collapse or by major mergers, whereas the outskirts of galaxies were likely formed after the formation of the bulge via different evolutionary channels (e.g., gas accretion or wet minor-mergers). Moreover, for the entire sample of galaxies our results also support the scenario in which galaxies form in an inside-out fashion.

8. SUMMARY AND CONCLUSIONS

Using the MaNGA sample (the largest IFU sample up to date, with $\approx$ 10000 galaxies), we present one of the most comprehensive explorations of the radial distribution of physical properties derived from both the stellar continuum and the ionized gas emission lines in the optical (including their main kinematic properties). From the entire sample we select a so-called *Golden Sample*, in other words, we select the closest targets with the best spatial coverage ($\approx$1400 galaxies). Given the size of the sample we are able to disentangle the impact of two fundamental global properties: the total stellar mass, M_* , and the morphology. To quantify the gradients of those radial distributions, we make use of a piecewise analysis allowing us to measure changes in the slope of those radial profiles as well as its characteristic value (i.e., measured at $R_{\rm eff}$). This allows us to quantify how the absolute values of a given property change depending on either the stellar mass or

the morphology. We also explore how these radial distributions vary when considering larger samples of galaxies at different distances (or physical spatial resolution) and with different spatial coverage ($\approx$ 7000 galaxies).

In general, we find that most of the physical properties from both components decrease with distance (e.g., Σ_*, and Hα flux) with M_* and the morphology, modulating their gradient as well as their characteristic values for some observables. Here we summarize the main results from this study for the different properties derived from the stellar continuum and ionized gas emission lines using the *Golden Sample*:

- The stellar mass surface density, Σ_*, as well as the stellar mass-to-light ratio, M/L, decrease with radius. Their slopes and characteristic values at $R_{\rm eff}$ become steeper and larger as M_* increases. Although morphology does not seem to significantly affect these slopes, the characteristic values for early-type galaxies are larger in comparison to late-type ones for a given bin of M_*. These results are in agreement with those derived for a heterogeneous sample of galaxies (Sánchez et al. 2021).

- Both the luminosity-weighted stellar age and metallicity show in general negative central slopes regardless of M_* and morphology. Although these gradients are close to flat, we find a mild trend with M_*, with the slopes becoming stepper as M_* increases. The characteristic values of both properties increase with M_*. Early-type galaxies are older and more metal rich in comparison to late-type galaxies of similar M_*. The central slope of the radial distribution of the stellar optical extinction, $\rm Av_{SSP}$, is close to zero for late-type galaxies and positive for early-type ones; external slopes are positive. The characteristic stellar extinction is significantly affected by morphology; late-type galaxies have larger values of $\rm Av_{SSP}$ in comparison to early-type object of similar M_*.

- The radial distributions of the flux from the brightest emission lines have a negative slope, with similar values for the probed lines. We do not find significant differences in their slope for different stellar mass or morphology. However, depending on the emission line, their fluxes at $R_{\rm eff}$ depend on M_* and morphology.

- From these emission lines we derive the radial distribution of their ratios. Depending on the ratio, the slope of the gradients can depend on both M_* and morphology. The Hα/Hβ line ratio allows us to estimate the optical extinction, $\rm Av_{gas}$ which in turn allows us to estimate the radial distribution of the molecular gas mass density, $\Sigma_{\rm mol,Av}$. We also present the radial distribution of properties derived from $\rm Av_{gas}$: $\rm Av_{gas}/Av_{SSP}$, and $f_{\rm mol}$. As explored by previous spatially resolved studies (Li et al. 2021), we find that the radial distribution of the $\rm Av_{gas}/Av_{SSP}$ ratio is not constant, but decreases with radius. Furthermore, the slope becomes steeper as M_* increases. On the other hand, $f_{\rm mol}$ has positive gradients regardless of M_* or the morphology.

- The slopes of the $\Sigma_{\rm SFR}$ gradients are negative with a similar value regardless of M_* or the morphology. On the other hand, the central slopes of the sSFR radial distribution have a mild variation from negative to positive, whereas the outer gradients have negative slopes. The slope of the gradient of SFE has negative values. For these three parameters, late-type galaxies have large characteristic values in comparison to early-type galaxies at similar M_*.

- We find that in general the radial gradients from the central portion of the oxygen abundance derived from emission-line calibrators have negative slopes. The exact values of those gradients depend on the calibrator. Contrary to previous studies, we do not find a strong impact of M_* on those gradients for late-type galaxies. The values of the oxygen abundance at $R_{\rm eff}$ strongly depend on both M_* and the adopted calibrator.

- The MaNGA dataset allows us to measure the radial distribution of the line-of-sight velocity from the stellar and ionized gas components. We find that, for both components, massive galaxies have a steeper increase in $V_{\rm los}$; these galaxies reach the expected plateau at smaller galactocentric distances in $V_{\rm los}$ than low-mass galaxies. Morphology also has a significant role in shaping those radial profiles: late-type galaxies have steeper gradients than those derived from early-type galaxies. On the other hand, the velocity dispersion of both components decreases with radius for the most massive galaxies, whereas for the low-mass galaxies the profiles are flat and close to 0 km/s.

- Using the kinematic information from each component we explore the radial distribution of the $V_{\rm los,H\alpha}/V_{\rm los,ssp}$ and $\sigma^{corr}_{\rm H\alpha}/\sigma_{\rm ssp}$ ratios. Although

the $V_{\rm los,H\alpha}/V_{\rm los,ssp}$ is relatively constant (close to unity) for different bins of M_* and morphology, we find that in the center of massive galaxies this ratio reaches values larger than 3. This is due to the large central value of $V_{\rm los,H\alpha}$ in comparison to $V_{\rm los,ssp}$ in early-type galaxies. On the other hand, the radial distribution of the $\sigma^{corr}_{\rm H\alpha}/\sigma_{\rm ssp}$ ratio varies significantly depending on both M_* and the morphology.

- In general, we find that the radial properties derived from the *Golden Sample* for the stellar and ionized gas components are similar to those derived from a larger low-inclined sample (≈7500 galaxies).

The radial distributions observed for the different parameters presented in this study are a significant evidence that the main processes responsible to shape the formation and evolution of galaxies appear to occur at kpc scales. These radial profiles are the result of the scaling relations derived at kpc scales; thus, at the same galactocentric distance the physics that regulates the properties of both the stellar component, the ionized gas, and the interplay between them is similar. Furthermore, these radial distributions suggest an inside-out formation scenario. Global properties, such as the stellar mass or morphology, play a secondary role in setting the local properties of galaxies in the local universe.

J.B-B acknowledges support from the grant IA-101522 (DGAPA-PAPIIT, UNAM) and funding from the CONACYT grant CF19-39578. L.C. thanks the support from the grant IN103820 (DGAPA-PAPIIT, UNAM). This research made use of Astropy,[11] a community-developed core Python package for Astronomy (Astropy Collaboration et al. 2013, 2018).

Funding for the Sloan Digital Sky Survey IV has been provided by the Alfred P. Sloan Foundation, the U.S. Department of Energy Office of Science, and the Participating Institutions.

SDSS-IV acknowledges support and resources from the Center for High Performance Computing at the University of Utah. The SDSS website is www.sdss.org.

SDSS-IV is managed by the Astrophysical Research Consortium for the Participating Institutions of the SDSS Collaboration including the Brazilian Participation Group, the Carnegie Institution for Science, Carnegie Mellon University, Center for Astrophysics — Harvard & Smithsonian, the Chilean Participation Group, the French Participation Group, Instituto de Astrofísica de Canarias, The Johns Hopkins University, Kavli Institute for Physics and Mathematics of the Universe (IPMU) / University of Tokyo, the Korean Participation Group, Lawrence Berkeley National Laboratory, Leibniz Institut für Astrophysik Potsdam (AIP), Max-Planck-Institut für Astronomie (MPIA Heidelberg), Max-Planck-Institut für Astrophysik (MPA Garching), Max-Planck-Institut für Extraterrestrische Physik (MPE), National Astronomical Observatories of China, New Mexico State University, New York University, University of Notre Dame, Observatário Nacional / MCTI, The Ohio State University, Pennsylvania State University, Shanghai Astronomical Observatory, United Kingdom Participation Group, Universidad Nacional Autónoma de México, University of Arizona, University of Colorado Boulder, University of Oxford, University of Portsmouth, University of Utah, University of Virginia, University of Washington, University of Wisconsin, Vanderbilt University, and Yale University.

[11] http://www.astropy.org

APPENDICES

A. RADIAL PROFILES AND GRADIENTS

In this Appendix we include the averaged radial profiles for the properties explored in this study. As we mention in § 2.4, we present these radial profiles for different bins of morphology and stellar mass.

B. OXYGEN ABUNDANCES USING DIFFERENT CALIBRATORS

As we mention in § 4.4.1, thanks to the `pyOxy` script, we are able to estimate the oxygen abundance using a large suite of strong-line calibrators. Although the script allows an estimation of the oxygen abundance for more than 20 calibrators, in this appendix we present the radial distribution and the piece-wise analysis using two of them, which we consider to be representative of this large set of calibrators: the empirical calibrator using the O3N2 ratio from Marino et al. (2013), and the theoretical calibrator using different line ratios proposed by Kobulnicky & Kewley (2004).

In Figure 56 we present the radial distribution of the oxygen abundance using the O3N2 abundance calibrator derived in Marino et al. (2013), whereas in Figure 58, we show the result from the piece-wise analysis of these radial profiles. In comparison to the results derived using the calibrator derived by Ho (2019, see Figure 22), we find that the central

gradients (k_0) using this O3N2 calibrator are flatter (and in some cases of opposite sign). The trend from k_0 for different bins of M_* for the Sb galaxies using the O3N2 calibrator is similar to those described by Belfiore et al. (2017): k_0 increases as M_* increases (except for the lowest-mass bin). However, for Sc galaxies we find that k_0 decreases with M_*. A similar trend is observed for Sd/Sm galaxies. For early-type galaxies we find flat gradients regardless of M_*. For the outskirts of galaxies the piece-wise analysis shows that the gradients ($k1$) change from positive to negative as M_* increases. This piece-wise analysis provides a more complete description of the radial gradients in comparison to assuming a single gradient to the entire radial distribution of the oxygen abundance (e.g., Sánchez-Menguiano et al. 2018). Finally, we find trends of the characteristic abundance using the O3N2 calibrator similar to those derive using the calibrator derived by Ho (2019). For late-type galaxies this abundance increases with M_* despite some variation among galaxies of this type: For a given stellar mass bin the oxygen abundance increases from Sd/Sm galaxies to Sb ones. For early-type galaxies the characteristic value of the oxygen abundance remains constant regardless of the morphological type (E/S0 or Sa) and M_* ($12 + \log(\mathrm{O/H}) \approx -8.5$).

In Figure 57 we present the radial distribution of the oxygen abundance using the O3N2 abundance calibrator derived in Kobulnicky & Kewley (2004), whereas in Figure 59, we show the result from the piece-wise analysis of these radial profiles. In general, we find results similar to those derived using the O3N2 calibrator.

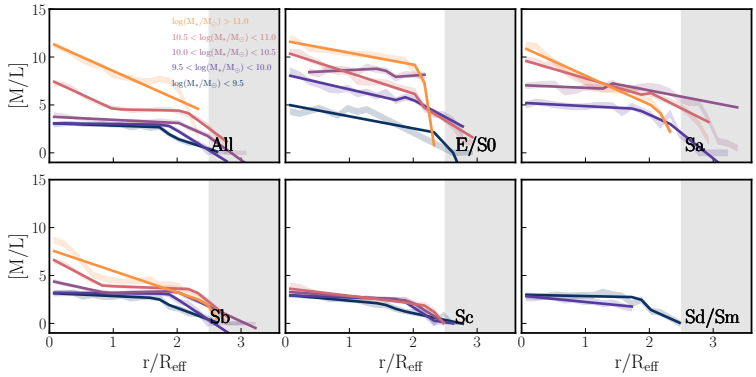

Fig. 33. Similar to Figure 3 for the M/L ratio. The gradients are averaged by morphology (panels from left to right and top to bottom) and total stellar mass bins (shaded colored areas; each color represents a stellar mass bin; see the legend at the top-left panel). The gray shaded area in each panel represents the typical maximum radius covered by the FoV ($R_{\rm eff} \approx 2.5$). The solid lines in each panel represent the best fit derived from fitting a piecewise function to the radial distribution. The color figure can be viewed online.

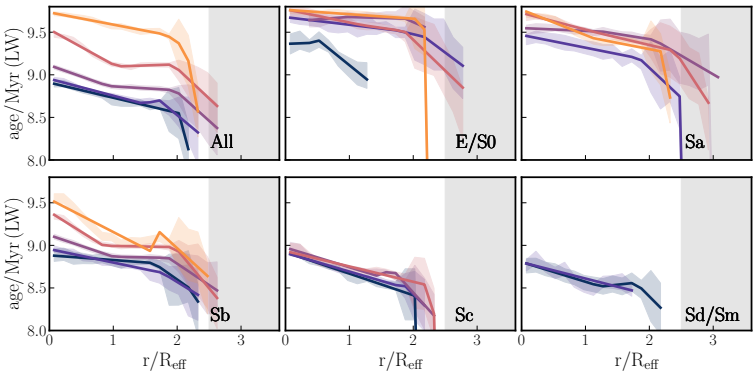

Fig. 34. Similar to Figure 3 for the luminosity-weighted age of the stellar population. The color figure can be viewed online.

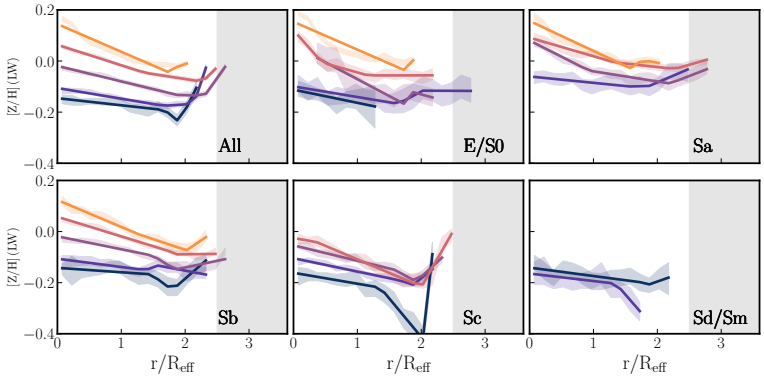

Fig. 35. Similar to Figure 3 for the luminosity-weighted stellar age. The color figure can be viewed online.

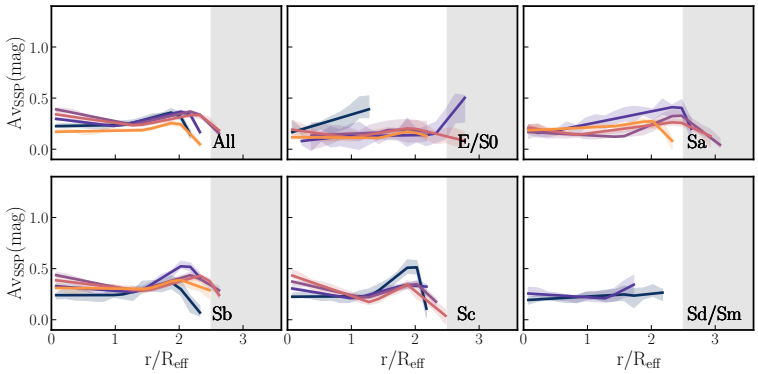

Fig. 36. Similar to Figure 3 for the luminosity-weighted stellar age. The color figure can be viewed online.

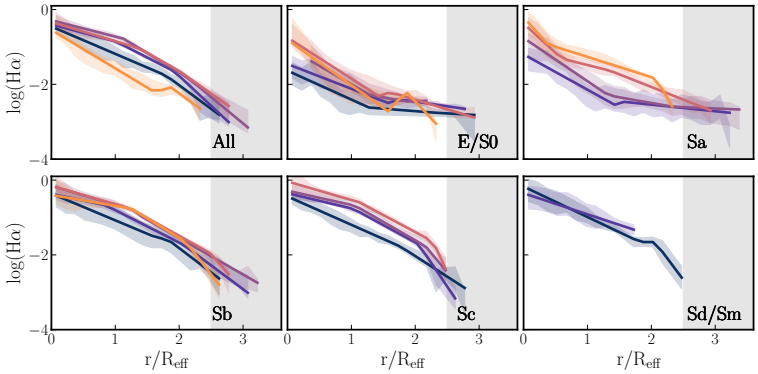

Fig. 37. Similar to Figure 3 for the Hα emission line. The color figure can be viewed online.

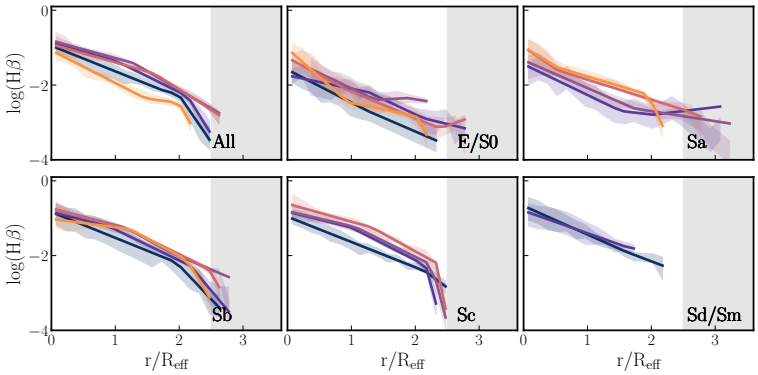

Fig. 38. Similar to Figure 3 for the Hβ emission line. The color figure can be viewed online.

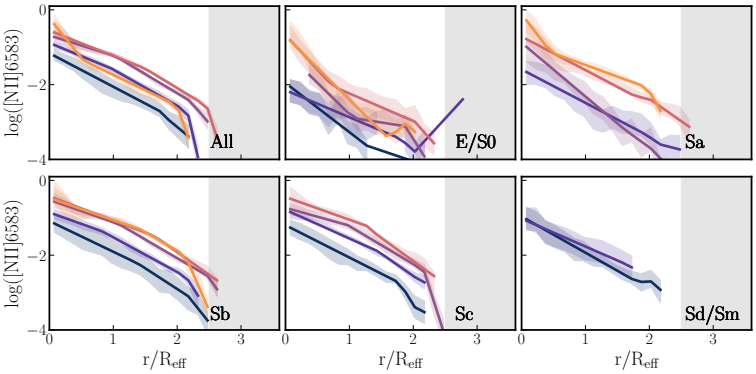

Fig. 39. Similar to Figure 3 for the [NII] emission line. The color figure can be viewed online.

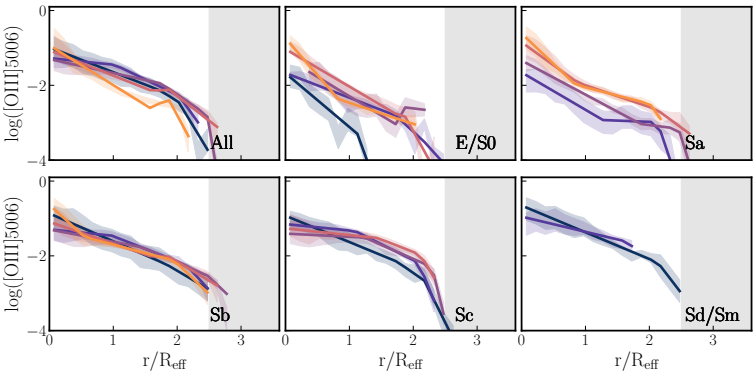

Fig. 40. Similar to Figure 3 for the [OIII] emission line. The color figure can be viewed online.

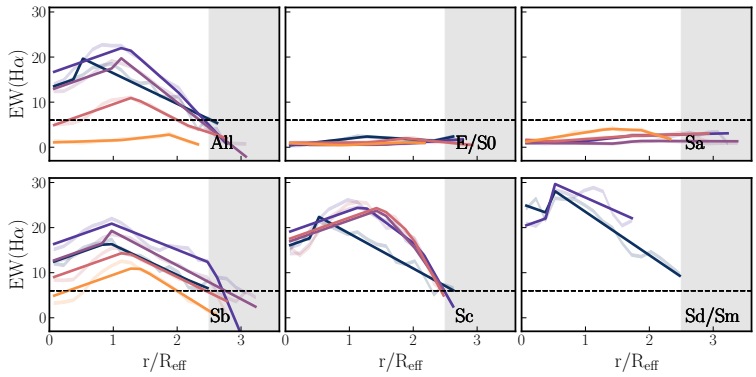

Fig. 41. Similar to Figure 3 for EW(Hα). The dashed horizontal lines in all the panels represent an EW(Hα) of 6Å. The color figure can be viewed online.

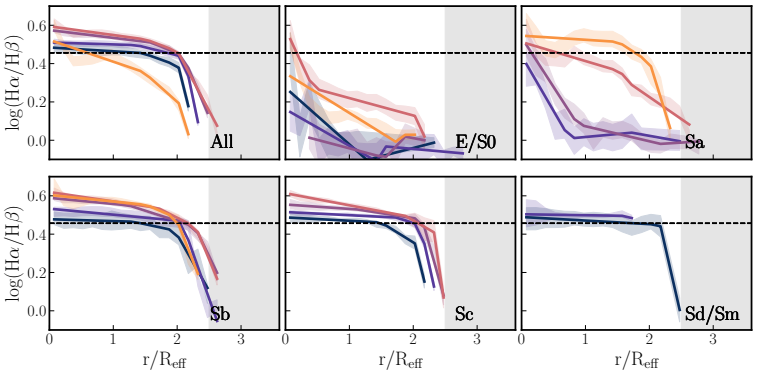

Fig. 42. Similar to Figure 3 for the Hα/Hβ line ratio. The dashed horizontal lines in all the panels represent the canonical value of this ratio. The color figure can be viewed online.

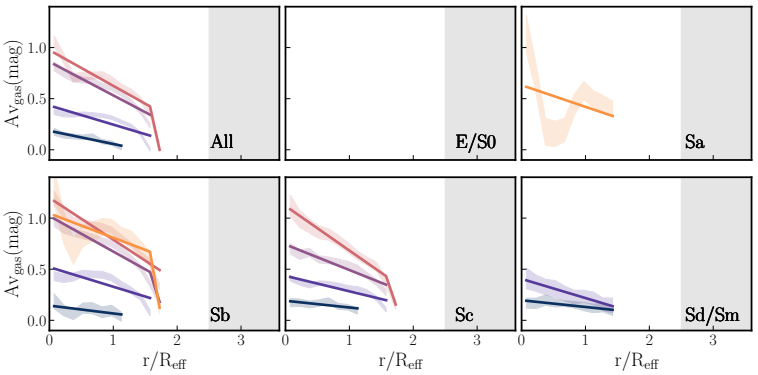

Fig. 43. Similar to Figure 3 for the optical extinction derived from the Balmer decrement. The color figure can be viewed online.

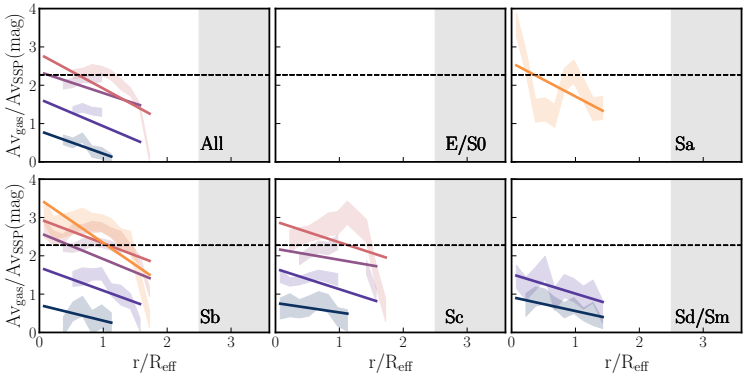

Fig. 44. Similar to Figure 3 for the Av_{gas} /Av_{SSP} ratio. The dashed line in all the panels represents the value derived from Calzetti (1997):Av_{gas} /$Av_{SSP} \approx 2.27$. The color figure can be viewed online.

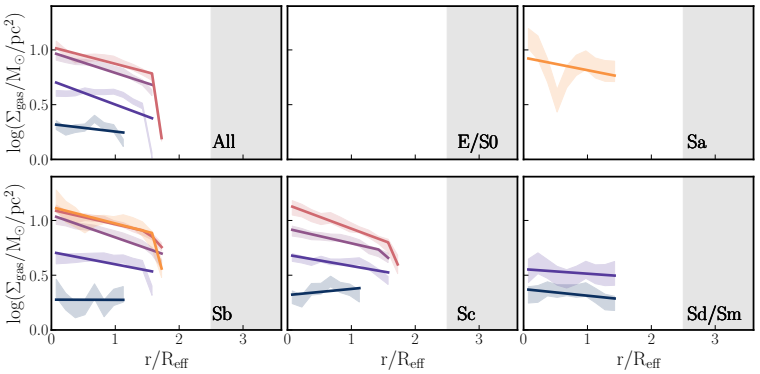

Fig. 45. Similar to Figure 3 for $\Sigma_{\rm mol,Av}$. The color figure can be viewed online.

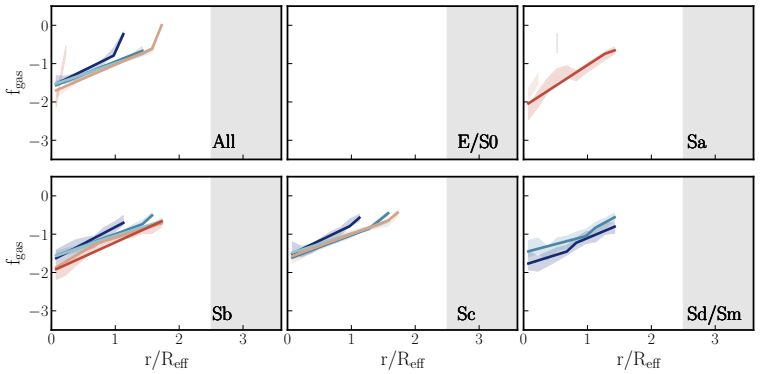

Fig. 46. Similar to Figure 3 for gas fraction, $\rm f_{mol}$. The color figure can be viewed online.

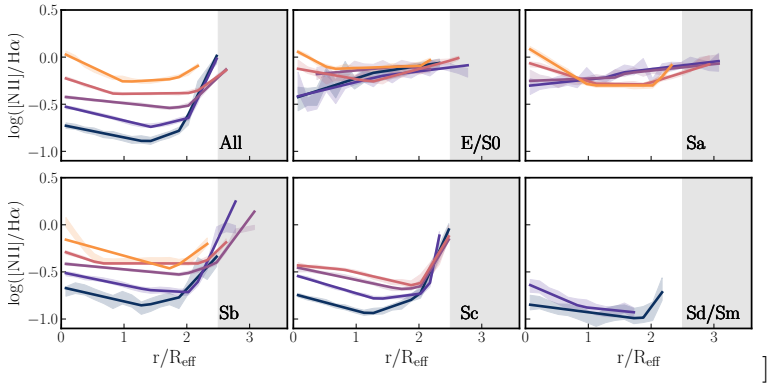

Fig. 47. Similar to Figure 3 for emission lines ratio [NII]/Hα. The color figure can be viewed online.

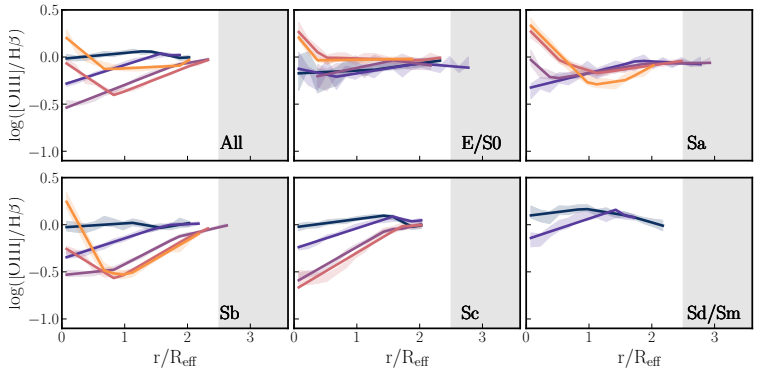

Fig. 48. Similar to Figure 3 for emission lines ratio [OIII]/Hβ. The color figure can be viewed online.

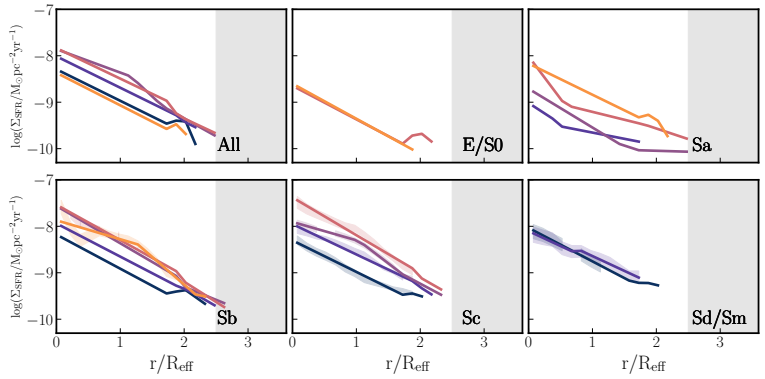

Fig. 49. Similar to Figure 3 for $\Sigma_{\rm SFR}$. The color figure can be viewed online.

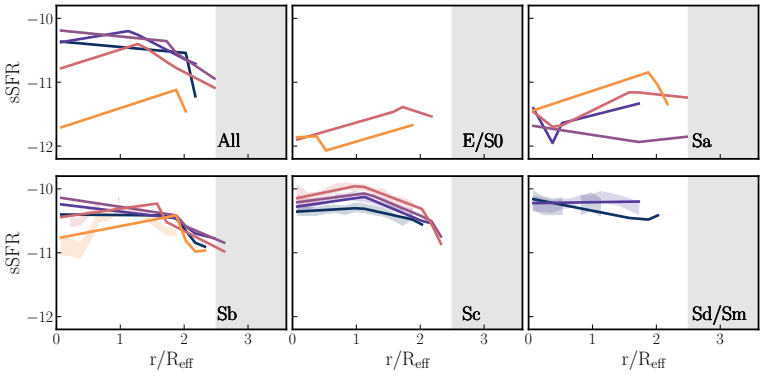

Fig. 50. Similar to Figure 3 for sSFR. The color figure can be viewed online.

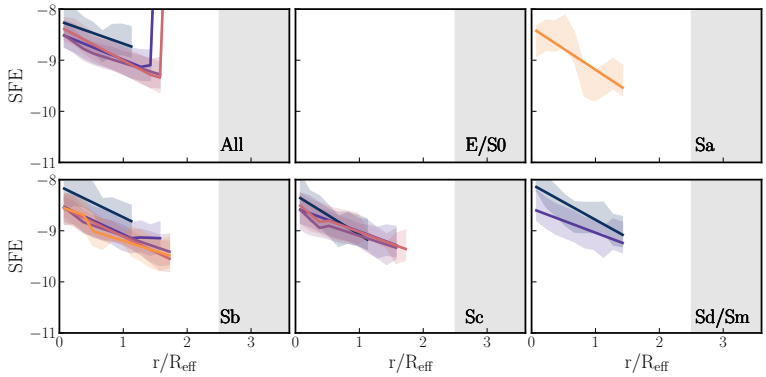

Fig. 51. Similar to Figure 3 for SFE. The color figure can be viewed online.

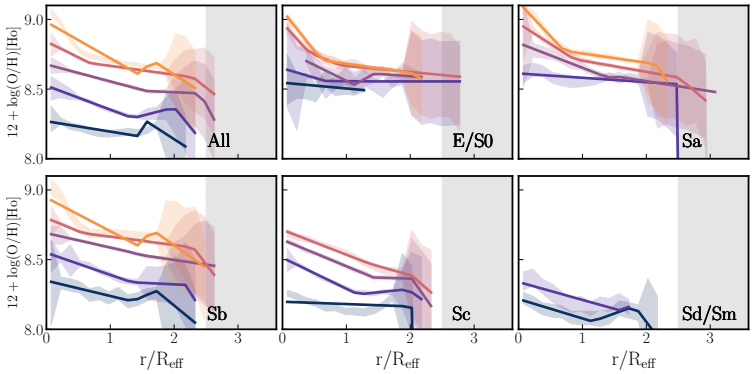

Fig. 52. Similar to Figure 3 for the oxygen abundance derived using the calibrator presented in Ho (2019). The color figure can be viewed online.

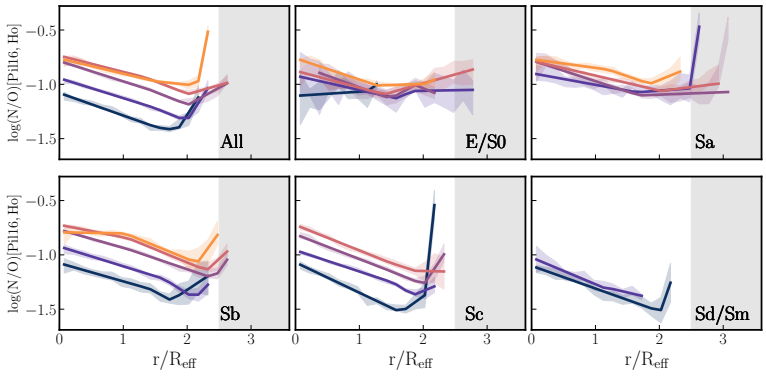

Fig. 53. Similar to Figure 3 for the N/O ratio. The color figure can be viewed online.

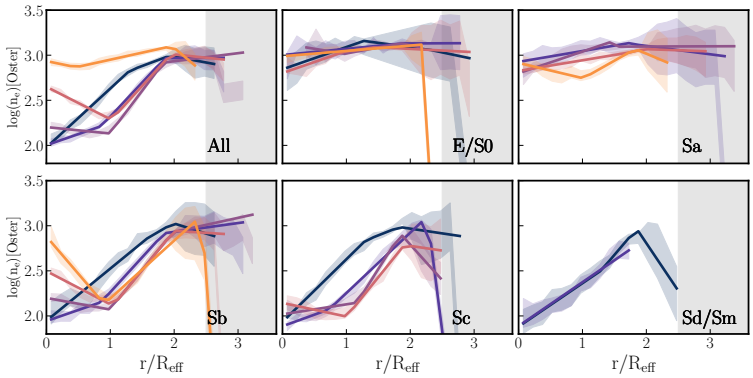

Fig. 54. Similar to Figure 3 for the electron density. The color figure can be viewed online.

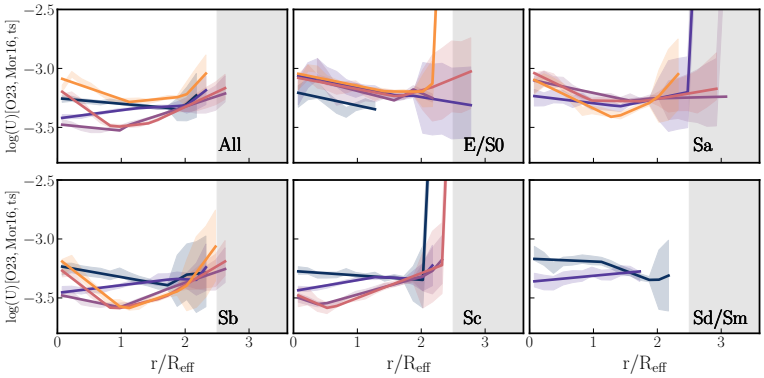

Fig. 55. Similar to Figure 3 for the ionization parameter. The color figure can be viewed online.

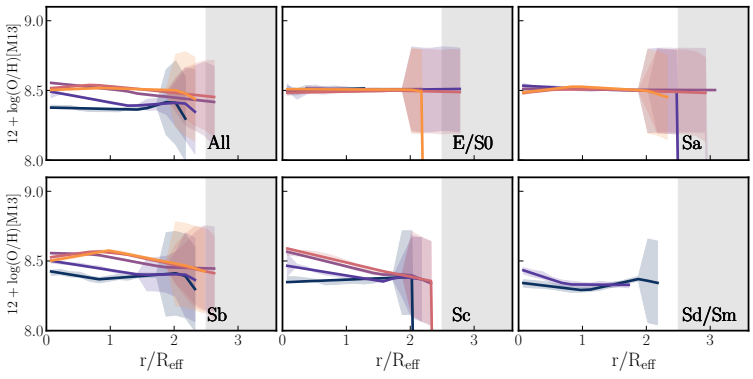

Fig. 56. Similar to Figure 3 for the oxygen abundance derived using the calibrator presented in Marino et al. (2013). The color figure can be viewed online.

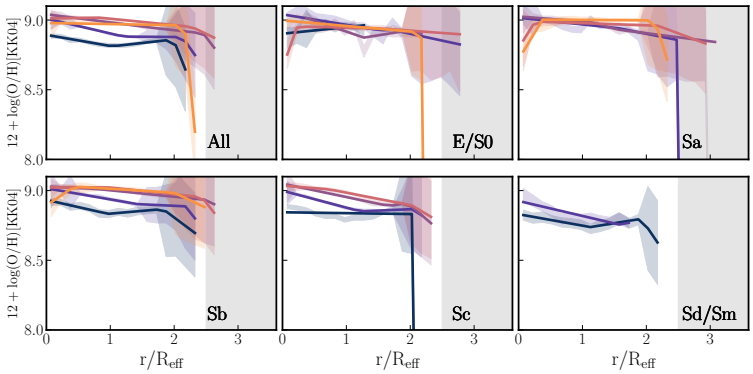

Fig. 57. Similar to Figure 3 for the oxygen abundance derived using the calibrator presented in Kobulnicky & Kewley (2004). The color figure can be viewed online.

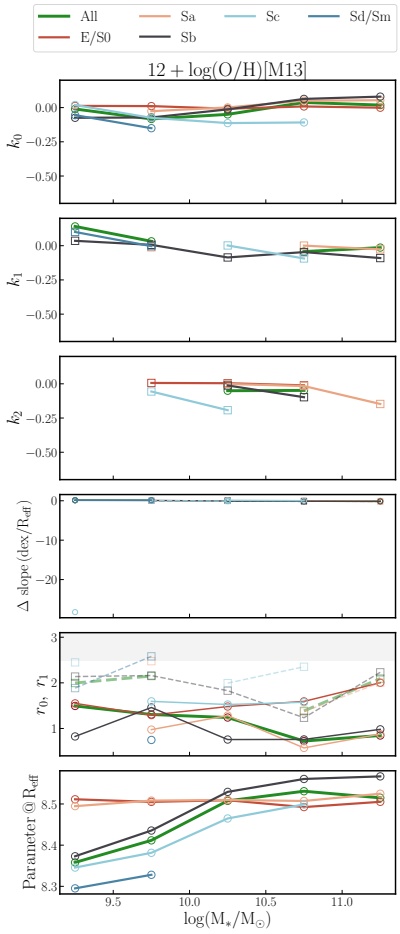

Fig. 58. Similar to Figure 3 for the oxygen abundance derived using the calibrator presented in Ho (2019). The color figure can be viewed online.

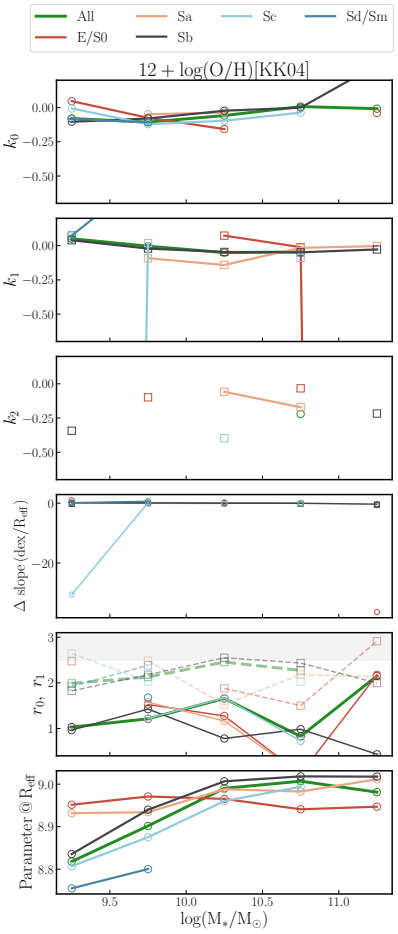

Fig. 59. Similar to Figure 3 for the oxygen abundance derived using the calibrator presented in Ho (2019). The color figure can be viewed online.

REFERENCES

Abdurro'uf, Accetta, K., Aerts, C., et al. 2022, ApJS, 259, 35, https://doi.org/10.3847/1538-4365/ac4414

Astropy Collaboration, Price-Whelan, A. M., SipHocz, B. M., et al. 2018, AJ, 126, 153, https://doi.org/10.3847/1538-3881/aabc4f

Astropy Collaboration, Robitaille, T. P., Tollerud, E. J., et al. 2013, A&A, 558, 33, https://doi.org/10.1051/0004-6361/201322068

Baldwin, J. A., Phillips, M. M., & Terlevich, R. 1981, PASP, 93, 5, https://doi.org/10.1086/130766

Barrera-Ballesteros, J. K., Heckman, T., Sánchez, S. F., et al. 2018, ApJ, 852, 74, https://doi.org/10.3847/1538-4357/aa9b31

Barrera-Ballesteros, J. K., Heckman, T. M., Zhu, G. B., et al. 2016, MNRAS, 463, 2513, https://doi.org/10.1093/mnras/stw1984

Barrera-Ballesteros, J. K., Sánchez, S. F., Heckman, T., et al. 2021, MNRAS, 503, 3643, https://doi.org/10.1093/mnras/stab755

Barrera-Ballesteros, J. K., Utomo, D., Bolatto, A. D., et al. 2020, MNRAS, 492, 2651, https://doi.org/10.1093/mnras/stz3553

Belfiore, F., Maiolino, R., Tremonti, C., et al. 2017, MNRAS, 469, 151, https://doi.org/10.1093/mnras/stx789

Bigiel, F., Leroy, A., Walter, F., et al. 2008, AJ, 136, 2846, https://doi.org/10.1088/0004-6256/136/6/2846

Binette, L., Magris, C. G., Stasińska, G., & Bruzual, A. G. 1994, A&A, 292, 13

Blanton, M. R., Bershady, M. A., Abolfathi, B., et al. 2017, AJ, 154, 28, https://doi.org/10.3847/1538-3881/aa7567

Blanton, M. R., Kazin, E., Muna, D., Weaver, B. A., & Price-Whelan, A. 2011, AJ, 142, 31, https://doi.org/10.1088/0004-6256/142/1/31

Boardman, N. F., Zasowski, G., Newman, J. A., et al. 2021, MNRAS, 501, 948, https://doi.org/10.1093/mnras/staa3785

Brinchmann, J., Charlot, S., White, S. D. M., et al. 2004, MNRAS, 351, 1151, https://doi.org/10.1111/j.1365-2966.2004.07881.x

Bundy, K., Bershady, M. A., Law, D. R., et al. 2015, ApJ, 798, 7, https://doi.org/10.1088/0004-637X/798/1/7

Calzetti, D. 1997, AIPC 408, The ultraviolet universe at low and high redshift, 403, https://doi.org/10.1063/1.53764

Calzetti, D., Armus, L., Bohlin, R. C., et al. 2000, ApJ, 533, 682, https://doi.org/10.1086/308692

Cano-Díaz, M., Ávila-Reese, V., Sánchez, S. F., et al. 2019, MNRAS, 488, 3929, https://doi.org/10.1093/mnras/stz1894

Cano-Díaz, M., Sánchez, S. F., Zibetti, S., et al. 2016, ApJ, 821, 26, https://doi.org/10.3847/2041-8205/821/2/L26

Cappellari, M. 2016, ARA&A, 54, 597, https://doi.org/10.1146/annurev-astro-082214-122432

Cardelli, J. A., Clayton, G. C., & Mathis, J. S. 1989, ApJ, 345, 245, https://doi.org/10.1086/167900

Catalán-Torrecilla, C., Gil de Paz, A., Castillo-Morales, A., et al. 2015, A&A, 584, 87, https://doi.org/10.1051/0004-6361/201526023

Cid Fernandes, R., Stasińska, G., Mateus, A., & Vale Asari, N. 2011, MNRAS, 413, 1687, https://doi.org/10.1111/J.1365-2966.2011.18244.x

Cid Fernandes, R., Stasińska, G., Schlickmann, M. S., et al. 2010, MNRAS, 403, 1036, https://doi.org/10.1111/j.1365-2966.2009.16185.x

Colombo, D., Sanchez, S. F., Bolatto, A. D., et al. 2020, A&A, 644, 97, https://doi.org/10.1051/0004-6361/202039005

Croom, S. M., Lawrence, J. S., Bland-Hawthorn, J., et al. 2012, MNRAS, 421, 872, https://doi.org/10.1111/j.1365-2966.2011.20365.x

de Vaucouleurs, G. 1958, ApJ, 128, 465, https://doi.org/10.1086/146564

Domínguez, A., Siana, B., Henry, A. L., et al. 2013, ApJ, 763, 145, https://doi.org/10.1088/0004-637X/763/2/145

Drory, N., MacDonald, N., Bershady, M. A., et al. 2015, AJ, 149, 77, https://doi.org/10.1088/0004-6256/149/2/77

Ellison, S. L., Thorp, M. D., Lin, L., et al. 2020, MNRAS, 493, 39, https://doi.org/10.1093/mnrasl/slz179

Emsellem, E., Cappellari, M., Krajnović, D., et al. 2007, MNRAS, 379, 401, https://doi.org/10.1111/j.1365-2966.2007.11752.x

Espinosa-Ponce, C., Sánchez, S. F., Morisset, C., et al. 2022, MNRAS, 512, 3436, https://doi.org/10.1093/mnras/stac456

Flores-Fajardo, N., Morisset, C., Stasińska, G., & Binette, L. 2011, MNRAS, 415, 2182, https://doi.org/10.1111/j.1365-2966.2011.18848.x

Freeman, K. C. 1970, ApJ, 160, 811, https://doi.org/10.1086/150474

Goddard, D., Thomas, D., Maraston, C., et al. 2017, MNRAS, 466, 4731, https://doi.org/10.1093/mnras/stw3371

González Delgado, R. M., García-Benito, R., Pérez, E., et al. 2015, A&A, 581, 103, https://doi.org/10.1051/0004-6361/201525938

Gunn, J. E., Siegmund, W. A., Mannery, E. J., et al. 2006, AJ, 131, 2332, https://doi.org/10.1086/500975

Ho, I.-T. 2019, MNRAS, 485, 3569, https://doi.org/10.1093/mnras/stz649

Husemann, B., Jahnke, K., Sánchez, S. F., et al. 2014, MNRAS, 443, 755, https://doi.org/10.1093/mnras/stu1167

Husemann, B., Sánchez, S. F., Wisotzki, L., et al. 2010, A&A, 519, 115, https://doi.org/10.1051/0004-6361/201014559

Ibarra-Medel, H. J., Avila-Reese, V., Sánchez, S. F., González-Samaniego, A., & Rodríguez-Puebla, A. 2019, MNRAS, 483, 4525, https://doi.org/10.1093/mnras/sty3256

Johnston, E. J., Häußler, B., Aragón-Salamanca, A., et al. 2017, MNRAS, 465, 2317, https://doi.org/10.1093/mnras/stw2823

Kauffmann, G., Heckman, T. M., White, S. D. M., et al. 2003, MNRAS, 341, 54, https://doi.org/10.1046/j.1365-8711.2003.06292.x

Kennicutt, R. C., Jr. 1992, ApJ, 388, 310, https://doi.org/10.1086/171154

_____. 1998, ARA&A, 36, 189, https://doi.org/10.1146/annurev.astro.36.1.189

Kennicutt, R. C., Jr. & Evans, N. J. II. 2012, ARA&A, 50, 531, https://doi.org/10.1146/annurev-astro-081811-125610

Kent, S. M. 1985, ApJS, 59, 115, https://doi.org/10.1086/191066

Kewley, L. J., Dopita, M. A., Sutherland, R. S., Heisler, C. A., & Trevena, J. 2001, ApJ, 556, 121, https://doi.org/10.1086/321545

Kobulnicky, H. A. & Kewley, L. J. 2004, ApJ, 617, 240, https://doi.org/10.1086/425299

Kormendy, J. 1977, ApJ, 217, 406, https://doi.org/10.1086/155589

Koyama, Y., Kodama, T., Hayashi, M., et al. 2015, MNRAS, 453, 879, https://doi.org/10.1093/mnras/stv1599

Koyama, Y., Shimakawa, R., Yamamura, I., Kodama, T., & Hayashi, M. 2019, PASJ, 71, 8, https://doi.org/10.1093/pasj/psy113

Kreckel, K., Groves, B., Schinnerer, E., et al. 2013, ApJ, 771, 62, https://doi.org/10.1088/0004-637x/771/1/62

Lacerda, E. A. D., Cid Fernandes, R., Couto, G. S., et al. 2018, MNRAS, 474, 3727, https://doi.org/10.1093/mnras/stx3022

Lacerda, E. A. D., Sánchez, S. F., Cid Fernandes, R., et al. 2020, MNRAS, 492, 3073, https://doi.org/10.1093/mnras/staa008

Lacerda, E. A. D., Sánchez, S. F., Mejía-Narváez, A., et al. 2022, https://doi.org/10.48550/arXiv.2202.08027

Law, D. R., Cherinka, B., Yan, R., et al. 2016, AJ, 152, 83, https://doi.org/10.3847/0004-6256/152/4/83

Law, D. R., Westfall, K. B., Bershady, M. A., et al. 2021, AJ, 161, 52, https://doi.org/10.3847/1538-3881/abcaa2

Leroy, A. K., Walter, F., Brinks, E., et al. 2008, AJ, 136, 2782, https://doi.org/10.1088/0004-6256/136/6/2782

Li, N., Li, C., Mo, H., et al. 2021, ApJ, 917, 72, https://doi.org/10.3847/1538-4357/ac0973

Lin, Z. & Kong, X. 2020, ApJ, 888, 88, https://doi.org/10.3847/1538-4357/ab5f0e

López-Cobá, C., Sánchez, S. F., Moiseev, A. V., et al. 2017, MNRAS, 467, 4951, https://doi.org/10.1093/mnras/stw3355

Maiolino, R. & Mannucci, F. 2019, A&A Rev., 27, 3, https://doi.org/10.1007/s00159-018-0112-2

Marino, R. A., Rosales-Ortega, F. F., Sánchez, S. F., et al. 2013, A&A, 559, 114, https://doi.org/10.1051/0004-6361/201321956

Martin, C. L. & Kennicutt, R. C., Jr. 2001, ApJ, 555, 301, https://doi.org/10.1086/321452

McCall, M. L., Rybski, P. M., & Shields, G. A. 1985, ApJS, 57, 1, https://doi.org/10.1086/190994

Méndez-Abreu, J., de Lorenzo-Cáceres, A., & Sánchez, S. F. 2021, MNRAS, 504, 3058, https://doi.org/10.1093/mnras/stab1064

Méndez-Abreu, J., Sánchez, S. F., & de Lorenzo-Cáceres, A. 2019, MNRAS, 484, 4298, https://doi.org/10.1093/mnras/stz276

Morelli, L., Corsini, E. M., Pizzella, A., et al. 2015, MNRAS, 452, 1128, https://doi.org/10.1093/mnras/stv1357

Morisset, C., Delgado-Inglada, G., Sánchez, S. F., et al. 2016, A&A, 594, 37, https://doi.org/10.1051/0004-6361/201628559

Moustakas, J., Kennicutt, R. C., Jr., & Tremonti, C. A. 2006, ApJ, 642, 775, https://doi.org/10.1086/500964

Osterbrock, D. E. & Ferland, G. J. 2006, Astrophysics of gaseous nebulae and active galactic nuclei (2nd ed.; Sausalito, CA: University Science Books)

Pagel, B. E. J. & Edmunds, M. G. 1983, Natur, 304, 488, https://doi.org/10.1038/304488a0

Parikh, T., Thomas, D., Maraston, C., et al. 2021, MNRAS, 502, 5508, https://doi.org/10.1093/mnras/stab449

Peletier, R. F. 1989, Eliptical galaxies: structure and stellar content, PhD. Thesis, University of Groningen

Pilyugin, L. S. & Grebel, E. K. 2016, MNRAS, 457, 3678, https://doi.org/10.1093/mnras/stw238

Portinari, L. & Salucci, P. 2010, A&A, 521, 82, https://doi.org/10.1051/0004-6361/200811444

Price, S. H., Kriek, M., Brammer, G. B., et al. 2014, ApJ, 788, 86, https://doi.org/10.1088/0004-637x/788/1/86

Qin, J., Zheng, X. Z., Wuyts, S., Pan, Z., & Ren, J. 2019, ApJ, 886, 28, https://doi.org/10.3847/1538-4357/ab4a04

Raga, A. C., Castellanos-Ramírez, A., Esquivel, A., Rodríguez-González, A., & Velázquez, P. F. 2015, RMxAA, 51, 231

Reddy, N. A., Kriek, M., Shapley, A. E., et al. 2015, ApJ, 806, 259, https://doi.org/10.1088/0004-637X/806/2/259

Renzini, A. & Peng, Y.-j. 2015, ApJ, 801, 29, https://doi.org/10.1088/2041-8205/801/2/L29

Sánchez, S. F. 2020, ARA&A, 58, 99, https://doi.org/10.1146/annurev-astro-012120-013326

Sánchez, S. F., Kennicutt, R. C., Gil de Paz, A., et al. 2012, A&A, 538, 8, https://doi.org/10.1051/0004-6361/201117353

Sánchez, S. F., Pérez, E., Sánchez-Blázquez, P., et al. 2016, RMxAA, 52, 21, https://doi.org/10.48550/arXiv.1509.08552

Sánchez, S. F., Pérez, E., Sánchez-Blázquez, P., et al. 2016, RMxAA, 52, 171, https://doi.org/10.48550/arXiv.1602.01830

Sánchez, S. F., Walcher, C. J., Lopez-Cobá, C., et al. 2021, RMxAA, 57, 3, https://doi.org/10.22201/ia.01851101p.2021.57.01.01

Sánchez-Blázquez, P., Rosales-Ortega, F., Diaz, A., & Sánchez, S. F. 2014a, MNRAS, 437, 1534, https://doi.org/10.1093/mnras/stt1984

Sánchez-Blázquez, P., Rosales-Ortega, F. F., Méndez-Abreu, J., et al. 2014b, A&A, 570, 6, https://doi.org/10.1051/0004-6361/201423635

Sánchez-Menguiano, L., Sánchez, S. F., Pérez, I., et al. 2018, A&A, 609, 119, https://doi.org/10.1051/0004-6361/201731486

Sersic, J. L. 1968, Atlas de Galaxias Australes (Cordoba, Argentina: Observatorio Astronómico)

Smee, S. A., Gunn, J. E., Uomoto, A., et al. 2013, AJ, 146, 32, https://doi.org/10.1088/0004-6256/146/2/32

Villanueva, V., Bolatto, A., Vogel, S., et al. 2021, ApJ, 923, 60, https://doi.org/10.3847/1538-4357/ac2b29

Wake, D. A., Bundy, K., Diamond-Stanic, A. M., et al. 2017, AJ, 154, 86, https://doi.org/10.3847/1538-3881/aa7ecc

Wild, V., Charlot, S., Brinchmann, J., et al. 2011, MNRAS, 417, 1760, https://doi.org/10.1111/j.1365-2966.2011.19367.x

Yan, R., Tremonti, C., Bershady, M. A., et al. 2016, AJ, 151, 8, https://doi.org/10.3847/0004-6256/151/1/8

Zheng, Z., Wang, H., Ge, J., et al. 2017, MNRAS, 465, 4572, https://doi.org/10.1093/mnras/stw3030

J. K. Barrera-Ballesteros, L. Carigi, C. Espinosa-Ponce, H. Hernandez-Toledo, E. Lacerda, A. Z. Lugo-Aranda, and S. F. Sánchez: Universidad Nacional Autónoma de México, Instituto de Astronomía, AP 70-264, CDMX 04510, México.

N. Boardman: School of Physics and Astronomy, University of St Andrews, North Haugh, St Andrews KY16 9SS, UK.

J. R. Brownstein: Department of Physics and Astronomy, University of Utah, 115 S. 1400 E., Salt Lake City, UT 84112, USA.

G. Bruzual: IRyA, Universidad Nacional Autónoma de México, Campus Morelia, Michoacan, México C.P. 58089, México.

N. Drory: University of Texas at Austin, McDonald Observatory, 1 University Station, Austin, TX 78712, USA.

Richard R. Lane: Centro de Investigación en Astronomía, Universidad Bernardo O'Higgins, Avenida Viel 1497, Santiago, Chile.

C. López-Cobá: Institute of Astronomy and Astrophysics, Academia Sinica, No. 1, Section 4, Roosevelt Road, Taipei 10617, Taiwan.